UNIVERSITY OF VALENCIA & CINVESTAV-IPN

Electronic and thermoelectric properties of InSe, GaSe and $InGaSe_2$ superlattices

BY

HANNAN ELSAYED SADEK ABDELGELIL

SUPERVISED BY

RITO DANIEL OLGUÍN MELO

ANDRES CANTARERO SAEZ

Valencia, SEPTEMBER 2017
PROGRAMA OFICIAL DE DOCTORADO EN FÍSICA 3026

Dr. Andrés Cantarero Sáez, Profesor Catedrático del Departamento de Física Aplicada de la Universidad de Valencia y Dr. Rito Daniel Olguín Melo Profesor del Departamento de Física de Centro de Investigación y de Estudios Avanzados del Instituto Politécnico Nacional en México.

CERTIFICAN:

Que la Memoria presentada por Dña. Hannan Elsayed Sadek Abdelgelil con título "Electronic and thermoelectric properties of InSe, GaSe, and InGaSe2 superlattices", ha sido realizada bajo su dirección en el Instituto de Ciencia Molecular de la Universidad de Valencia y Centro de Investigación y de Estudios Avanzados del Instituto Politécnico Nacional en Mexico, autorizando mediante este escrito la presentación de la misma para optar al grado de Doctor en física.

Valencia, Septiembre de 2017.

Dr. Andrés Cantarero Sáez. Dr. Rito Daniel Olguín Melo.

إلي أمي

To my Mom:

My mother always says that I'm her dream,
but she doesn't know that she is my hero.

Acknowledgements

Since the first day I arrived to Spain and went through the investigation field, I knew that the way wouldn't be easy. But I always believed that with the help of the other people and their company can pave even the hardest paths. So, I wanted to thank all the people who have been part of my journey till I finish this stage of my life.

At first I want to express my deepest gratitude to the my research supervisors, Prof. Andrés Cantarero and Prof. Daniel Olguín, for their continuous encouragement, helpful suggestions, valuable supervision, and reading throughout the manuscript which have rendered the realization of this work to be possible.

I want to express my sincere gratitude to all the members in the CINVESTAV especially in the department of nano-science and nano-technology and the director of the department Dr. Jose Gerardo Cabanas for helping me during my stay in Mexico.

Great thanks to Mr. Magdi Abdelaziz for encouraging and helping me to not to leave my dream.

When we are far from our country, we need something that can remind us by the smell of home. Having a lot of Arab friends was always relieving the Symptoms of nostalgia. Thanks to all my Arab friends; Abeer, Afaf, Chiraz, Tarek, Mohamed, Ramy, Hadeer, Monay, Ahmed, Asmaa, Shimaa, Inas, Najaat, Dhikra, Zoulikha, Amal, Aya, Noha, Hasna, Zahra, Meriem, Amira, and Halima. The last period could be more complicated if you haven't been by my side, thanks to both of you Mai and Imen.

I would like to express my appreciation to my friends in the ICMUV and ICMOL institutes, María José, Maribel, Pedro, Pascual, Carlos, Mario and Daniel for their faithful help and kind cooperation.

Also I would like to thank my friends in Mexico, María, May, Farida, Odisey, July, Luz, Andrea, Fernanda, and Daladier.

Gracias tambien a mi familia española: Pilar, Amparo, Toñi, Santiago, Oleg y a todos los Estudiantes en la residencia por su apoyo y todo el amor que me han dado.

To my lovely friend in Egypt, Aya Mohamed Mekawy.

I'd like to express my gratitude and love to my father, mother, my lovely sisters; Shimaa and Sara, my brothers in law; Mahmoud and Hamada, and their little angels; Seba, Mohamed, Mohamed and Malek. They have always been my greatest support in this life.

Lastly, to my little brother, **Sadek**. It is hard to find someone who will stay believing in you at the moment when even you can't believe in yourself. The one who has never gotten tired of your complaints and you know for certain that he is never going to leave you alone even if he doesn't agree with you. I know that I'm very lucky in this world just for having this one in all the stages of my life. Grateful for having you always by my side in spite of the distance.

Contents

List of Figures

List of Tables

Chapter 1

General Introduction

There is a global energy crisis due to the vast consumption of non-renewable energy resources, fossil fuel, and to the continuous growth of the World Economy and industrial development. Some reports reveal that oil and gas reserves may diminish in the coming 50 years [1]. At the same time, our climate is affected by the burning of fossil fuels due to the emissions of the carbon dioxide that have passed the record level in the last decade, the so called Global Warming. To solve these problems, there is an urgent need to search for alternative, low cost, efficient and environmental friendly energy technologies such as photovoltaics, wind, bio fuels and thermoelectric energy conversion devices [2–5]. The interest in the development of thermoelectric devices comes from the fact that over 60% of the energy consummed in the World is lost as heat in most of the energy conversion processes. The waste heat can be converted directly into electrical energy using thermoelectric materials. Over the past decades, there has been a growing interest in exploring efficient thermoelectric materials [6–8] for power generation due to their potential application, many attractive features, such as no vibrations and noise (passive devices), high reliability and long service life. In thermoelectric power generators, heat energy is used to push electrons and holes in opposite directions in thermoelectric materials.

The work presented in this thesis focuses on the calculations of

the electrical and thermoelectric properties of some $III-VI$ compounds aimed at improving their efficiency for thermoelectric energy conversion. This chapter provides the background information on the thermoelectric effects and materials.

1.1 Thermoelectric effects

In a thermoelectric device, the voltage/current is generated from a thermal gradient via the Seebeck effect or a thermal gradient is created from the voltage difference via the Peltier effect due to the motion of the charge carriers inside the materials.

1.1.1 Seebeck Effect

Thomas Johann Seebeck noticed the deflection of a compass magnet close to a circuit made from two different materials that were joined in two places with a temperature difference between the junctions. At first, Seebeck thought that the deflection could be due to magnetism induced by the temperature difference. Then it was realized the generation of an electrical current due to the potential difference induced between the two junctions. The current deflect the magnet by Ampère's law. This phenomenon is known as the Seebeck effect. Figure 1.1 shows a schematic diagram of this effect where a voltage difference is created across the terminals of an open circuit made from a pair of dissimilar metals, A and B, whose two junctions are kept at different temperatures.

At a microscopic level, this could be explained by the higher thermal velocities of the charge carriers in the hot side of the materials with respect to the cold side. Then, they will diffuse from the hot to the cold side more quickly than in the opposite direction [9, 10]. If a thermal gradient is maintained across the material, a continuous flow of charge carriers gives rise to a voltage difference between the two sides. This is due to the fact that in the warmer side there is an excess of carriers as compared to the colest part

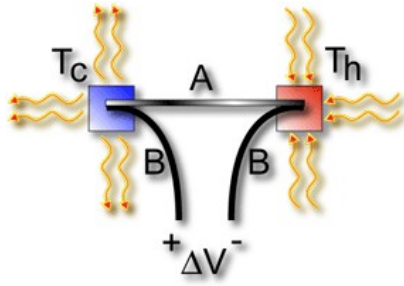

FIGURE 1.1: The voltage difference, ΔV, produced across the terminals of an open circuit made from a pair of dissimilar metals, A and B, whose junctions are kept at different temperatures, is directly proportional to the temperature difference $\Delta T = T_h - T_c$ between the hot and cold junction temperatures.

and the carriers are diffuse in order to be homogeneous through the material. The voltage difference ΔV is proportional to the temperature difference ΔT between the hot and cold sides of the junction;

$$\Delta V = -S\Delta T \tag{1.1}$$

The constant of proportionality S is termed as Seebeck coefficient or thermopower. Even though the term thermopower is a misnomer since it measures the voltage or electric field (actually the electromotive force) induced in response to a temperature difference, not the electric power. It has the units of V/K, though in practice it is more common to use microvolts per Kelvin, μV/K. The Seebeck coefficient depends on the crystal structure of the materials and the conductive properties. It has low values in metals as both the electrons and holes contribute to the induced thermoelectric voltage, hence they cancel the contributions of each others to the voltage, Whereas semiconductors can be doped with an excess amount of electrons or holes and thus can have large positive or negative values of the thermopower depending on type of the charge carriers. Thus the sign of the thermopower can determine if the semiconductor is $n-$ or $p-type$.

1.1.2 Peltier Effect

This is the reverse of the Seebeck effect and it bears the name of the physicist who has discovered it, Jean-Charles Peltier. He found that the flow of electric current through a junction between two dissimilar metals can produce heating or cooling. Thus, the heat is absorbed in one junction, and rejected in the other junction. The Peltier coefficient Π is defined as the heat transfered per unit of the applied current and is described mathematically by the equation [9, 11]:

$$\Pi = \frac{Q}{I} \quad , \tag{1.2}$$

where I is the electrical current and Q is the rate of heating or cooling.

1.1.3 Thomson Effect

In 1851, Lord Kelvin has predicted the Thomson Effect that comprises both the Seebeck and Peltier effects. It describes the heating or cooling of a homogeneous conducting material due to current passing through it as a result of a thermal gradient [12]. The rate of heating or cooling is proportional to both the electric current and the temperature gradient. The proportionality constant, known as the Thomson coefficient $\mathcal{K}$ is related by thermodynamics to the Seebeck coefficient. The relations with the Seebeck and Peltier coefficients are [13]:

$$\mathcal{K} = \frac{dS}{d\ln T} = \frac{d\Pi}{dT} - S \tag{1.3}$$

1.2 Thermoelectric material properties

The efficiency of a thermoelectric device is determined by its geometry and the intrinsic properties of the thermoelectric materials, giving usually in terms of the dimensionless thermoelectric

figure of merit ZT,

$$ZT = \frac{\sigma S^2}{\kappa} T \quad , \tag{1.4}$$

where σ is the electrical conductivity, S the Seebeck coefficient and κ the thermal conductivity that consists of two parts: the lattice thermal conductivity κ_l and the electronic conductivity κ_e.

The search for new thermoelectric materials seeks to maximize the power factor σS^2 and minimize the thermal conductivity κ [14–18]. It is difficult to find new compounds with large values of ZT since the electronic parameters in equation 1.4 are interrelated. Certainly, for higher ZT a low thermal conductivity is desired to maintain large temperature gradients. As the thermal conductance depends on heat transfer by both phonons and electrons, then a high electrical conductivity produces a high electronic thermal conductivity as well [19–26]. This relationship is represented by the Wiedemann-Franz law, strictly valid for metals. The law states that the ratio of the electronic part of the thermal conductivity of a material to its electrical conductivity is directly proportional to the temperature at which the properties are measured.

$$\frac{\kappa_e}{\sigma} = LT \tag{1.5}$$

The proportionality constant L is the Lorentz number and T the absolute temperature. Moreover, the Seebeck coefficient S and the electrical conductivity σ are coupled through the carrier concentration n. An increase in n decreases S, but σ increases with n [27–29]. Also the large value of the thermal conductivity will decrease the value of the Seebeck coefficient due to the difficulty of maintaining a high thermal gradient. Consequently, the interdependence have limited the selection of materials for thermoelectric applications. Metals have a high electrical conductivity σ and a small value of the Seebeck coefficient S Hence, the overall ZT remains low. On the contrary, semiconductors and semi-metals exhibit large Seebeck coefficient and relatively high σ and lower κ that may lead to the optimum ZT value [30].

Different strategies have been adopted to improve ZT. Since the

Seebeck coefficient and electrical conductivity are strongly dependent on the geometry of the band structure, band engineering is regarded as one of the most efficient approaches to develop high performance thermoelectric materials. The Seebeck coefficient could be improved by manipulating the density of states via band engineering through the introduction of resonant impurity states near the Fermi level [31, 32] or convergence of degenerate electronic bands by alloying [27, 33]. Also the lattice thermal conductivity can be reduced through phonon engineering by alloying or using layered structures [23, 34]. In 1993, Hicks [35, 36] theoretically predicted that S^2 increases linearly with decreasing the thickness because of the quantum confinement effect. Hence, ZT can be enhanced in the low dimensional materials [8, 37–39]

In this thesis we predict and report semiconductor materials which show a high Seebeck coefficient. Our results show that the Seebeck coefficient of these materials can be enhanced at room temperature by changing chemical potential.

1.3 Objectives and structure of the thesis

The main purpose of this work is to look for new thermoelectric materials with good transport properties that could be implemented in thermoelectric devices. Hence, in this thesis a comprehensive study of the electrical and thermoelectric properties of InSe, GaSe and $InGaSe_2$ superlattices have been presented. The thesis have been organized as follow:

- Chapter 1 displays a general introduction about thermoelectrics.
- Chapter 2 presents a brief description of the theories and the codes used in the calculations.
- Chapter 3 focuses on the structural and electronic properties of InSe and GaSe for the bulk and monolayer case calculated using the WIEN2k code that based on the density functional theory.

- Chapter 4 presented the study of the structural and electronic properties of a new superlattice that we propose here, $InGaSe_2$, for the bulk and mono layer case using the same procedure as in chapter 3.
- Chapter 5 focuses on a comparison between the results of the calculated transport properties of the three studied materials in both the bulk and monolayer case at room temperature. The calculations have been done using the Boltzmann transport theory as implemented in the BoltzTraP code.
- Chapter 6 showed the effect of three different pressure 0, 10, 20 GPa on the transport coefficient of the bulk case in the three studied materials.
- Chapter 7 summarizes the main conclusions of this work.
- Finally, a Spanish summary of the thesis work is presented in Chapter 8.

Chapter 2

Theory

2.1 Density functional theory (DFT)

The density functional theory is based on the assumption that all the properties of a system of many interacting particles can be viewed as functionals of the ground state density $n_0(\mathrm{r})$. Hence, all the information in the many-body wave functions for the ground state and all the excited states can be determined by the scalar function of positions $n_0(r)$. The DFT has been established in 1964 by two theorems due to Hohenberg and Kohn [40]. In these theorems the existence proofs for such functionals is given. However, they provide no guidance for constructing the functionals, and no exact functionals are known for any system of more than one electron.

Then the Ansatz made by Kohn and Sham [41] in 1965 turned DFT into a practical tool by providing a way to make useful, approximate ground state functionals for real systems of many electrons.

The interest in the density functional theory as the most promising approach for accurate, practical methods in the theory of materials was due to the remarkable successes of the approximate local density(LDA) and generalized-gradient approximation(GGA) functionals within the Kohn-Sham approach.

2.1.1 The quantum many body problem

The solid is a collection of heavy positively charged particles, nuclei, and lighter negatively charged particles, electrons. If there is N nuclei in the solid, hence there is electromagnetic interactions between N nuclei and ZN electrons, where Z is the atomic number. This is a many body problem that should be explained by quantum mechanics due to the existence of electrons. The Hamiltonian of this system is described by the equation

$$\begin{aligned}\hat{H} = &\frac{1}{2}\sum_{I}\frac{\hbar^2\boldsymbol{\nabla}_I^2}{M_I} + \frac{1}{2}\sum_{i}\frac{\hbar\boldsymbol{\nabla}_i^2}{m_i} + \frac{1}{2}\sum_{I,J}\frac{e^2}{|\boldsymbol{R}_I - \boldsymbol{R}_J|} \\ &+ \sum_{i\neq j}\frac{e^2}{|\boldsymbol{r}_i - \boldsymbol{r}_j|} + \sum_{i,I}\frac{e^2}{|\boldsymbol{R}_I - \boldsymbol{r}_j|} \quad ,\end{aligned} \tag{2.1}$$

where the kinetic and Coulomb interaction between all the ions and electrons in the solid have been taken into account. This Hamiltonian has several simplifications in Solid State Physics like the well known Bohr-Oppenheimer approximation [42]. Due to the fact that the nuclei are heavier than the electrons in this approximation the nuclei are assumed to be frozen at fixed positions and the electrons are in instantaneous equilibrium with them. This simplify the problem to be the problem of a collection of NZ interacting negative particles, moving in the external potential of the nuclei. Hence the Hamiltonian 2.1 of the system is reduced to be:

$$\hat{H} = \frac{\hbar}{2m_e}\sum_{i}\nabla_i^2 + \sum_{i}V_{ext}(\boldsymbol{r}_i) + \frac{1}{2}\sum_{i\neq j}\frac{e^2}{|\boldsymbol{r}_i - \boldsymbol{r}_j|} + E_{II} \quad , \tag{2.2}$$

as the kinetic energy of the nuclei now equal Zero and the Coulomb interaction between nuclei and other nuclei reduced to a constant.

2.1.2 The Hohenberg and Kohn theorems

After using the Bohr-Oppenheimer approximation, the problem is simpler than before but still too difficult to be solved. Now, the density functional theory could be used to simplify the problem of any system of interacting particles in an external potential $V_{ext}(\boldsymbol{r})$ and reduce equation 2.2 to an approximate but tractable form. The approach of Hohenberg and Kohn is to formulate the density functional theory as an exact theory for a many-body systems. The formulation of the Density functional theory is based upon two theorems, proved by Hohenberg and Kohn:

Theorem I : For any system of interacting particles in an external potential $V_{ext}(\boldsymbol{r})$, there is a one-to-one correspondence between the ground-state particle density $n_0(\boldsymbol{r})$ and the external potential. It means that the potential is determined uniquely by the ground state density. Consequently, the Hamiltonian is fully determined and hence the many body wavefunctions for all states (ground and excited) are determined. Therefore all properties of the system are completely determined given only the ground state density $n_0(\boldsymbol{r})$ since the ground-state expectation value of any observable $\hat{O}$ is a unique functional of the exact ground-state electron density:

$$\langle \Psi | \hat{O} | \Psi \rangle = O[n] \tag{2.3}$$

Theorem II: For $\hat{O}$ being the Hamiltonian $\hat{H}$ hence a universal functional for the energy $E[n]$ in terms of the density $n(\boldsymbol{r})$ can be defined, valid for any external potential $V_{ext}(\boldsymbol{r})$. For any particular $V_{ext}(\boldsymbol{r})$, the exact ground state energy of the system is the global minimum value of this functional, and the density $n(\boldsymbol{r})$ that minimizes the functional is the exact ground state density $n_0(\boldsymbol{r})$. As mentioned before that all properties can be viewed as a functional of $n(\boldsymbol{r})$ then the total energy functional is given by:

$$E_{HK}[n] = T[n] + E_{int}[n] + \int d^3r V_{ext}(\boldsymbol{r}) n(\boldsymbol{r}) + E_{II} \quad , \tag{2.4}$$

Where E_{II} is the interaction energy of the nuclei. The first two terms represent all internal energies, kinetic and potential, of the

interacting electrons system. Which must be universal by construction since the kinetic energy and interaction energy of the particles are functionals only of the density.

2.1.3 The Kohn-Sham Ansatz

The approach of Kohn and Sham is a practical procedure to obtain the ground state density via the replacement of the original many body problem by an auxiliary independent particle problem. This Ansatz leads to the exact solution of the properties of many-body systems using independent-particle methods. As a self-consistent method, the Kohn-Sham approach involves independent particles but an interacting density.

The Kohn-Sham approach is to replace the difficult interacting many-body system obeying the Hamiltonian 2.2 with an auxiliary system that can be solved more easily. In this approach the ground state density of the original interacting system is assumed to be equal to that of a selected non-interacting system. This leads to independent-particle equations for the non-interacting system that can be solved easily while all the difficult many-body terms are incorporated into an exchange-correlation functional of the density. Hence, the ground state density and energy of the original interacting system can be obtained by solving the Kohn-Sham equations and the accuracy will be limited only by the approximations used for the exchange-correlation functional.

Thus, the Kohn-Sham approach Ansatz rests upon two assumptions:

1. The ground state density of the original many body system can be replaced by the ground state density of an auxiliary system of non interacting particles.
2. The calculations are performed on the auxiliary independent-particle system that is defined by the auxiliary Hamiltonian. This Hamiltonian consists of the usual kinetic operator and an effective local potential $V^{\sigma}_{eff}(\boldsymbol{r})$ acting on

an electron of spin σ at point $\boldsymbol{r}$.

$$\hat{H}^{\sigma}_{aux} = -\frac{1}{2}\nabla^2 + V^{\sigma}(r) \tag{2.5}$$

The Kohn-Sham approach to the full interacting many-body problem consists of rewriting the Hohenberg-Kohn expression for the ground state energy functional in the form:

$$E_{KS} = T_s[n] + \int dr V_{ext}(r) n(r) + E_{Hartree}[n] + E_{II} + E_{xc}[n] \quad . \tag{2.6}$$

Here $V_{ext}(\boldsymbol{r})$ is the external potential due to the nuclei and any other external fields and E_{II} is the Coulomb interaction between the nuclei. T_s the independent particle kinetic energy is given by

$$T_s = -\frac{1}{2}\sum_{\sigma}\sum_{i=1}^{N^{\sigma}}(\psi_i^{\sigma}|\nabla^2|\psi_i^{\sigma})\frac{1}{2}\sum_{\sigma}\sum_{i=1}^{N^{\sigma}}|\nabla\psi_i^{\sigma}|^2 \tag{2.7}$$

$E_{Hartree}[n]$ the Hartree energy, the classical Coulomb interaction energy of the electron density $n(r)$ interacting with itself, is given by

$$E_{Hartree}[n] = \frac{1}{2}\int d^3\boldsymbol{r} d^3\boldsymbol{r}' \frac{n(\boldsymbol{r})n(\boldsymbol{r}')}{|\boldsymbol{r}-\boldsymbol{r}'|} \tag{2.8}$$

It means that all the many-body effects of exchange and correlation are grouped into the exchange correlation energy E_{xc}.

Comparing the Hohenberg-Kohn 2.4 and Kohn-Sham 2.6 expressions for the total energy shows that E_{xc} can be written as:

$$E_{xc}[n] = \langle\hat{T}\rangle - T_s[n] + \langle\hat{V}_{int}\rangle - E_{Hartree}[n] \quad . \tag{2.9}$$

Thus E_{xc} is just the difference of the kinetic and internal interaction energies of the true interacting many-body system from those of the fictional independent-particle system with electron-electron interactions replaced by the Hartree energy. If the universal functional $E_{xc}[n]$ was known then the Kohn-Sham equations for independent particles could be solved. From the solution the

exact ground state energy and density of the many-body electron problem could be found since The density of the auxiliary system is given by sums of squares of the orbitals $\psi_i^\sigma(\boldsymbol{r})$ for each spin σ.

$$n(\boldsymbol{r}) = \sum_\sigma n(\boldsymbol{r}, \sigma) = \sum_\sigma \sum_{i=1}^{N^\sigma} \left|\psi_i^\sigma(\boldsymbol{r})\right|^2 \tag{2.10}$$

If an approximation to $E_{xc}[n]$ describes the true exchange-correlation energy, then the Kohn-Sham method provides an appropriate approach to calculate the ground state of a many-body electron system.

2.1.4 The local density approximation

The only approximation that was made till now is the Born-Oppenheimer approximation after that no approximations were made. To define the exchange-correlation functional an approximation should be made. In the work of Kohn-Sham, they mentioned that solids can often be considered as close to the limit of the homogeneous electron gas. In that limit, it is known that the effects of exchange and correlation are local in character and they proposed making the local density approximation (LDA). This approximation postulates that the exchange-correlation functional has this form:

$$E_{xc}^{LDA} = \int n(\boldsymbol{r}) \epsilon_{xc}^{hom}(n) d^3\boldsymbol{r} \tag{2.11}$$

,where ϵ_{xc}^{hom} is the exchange correlation energy of the homogeneous electron gas. It means that the exchange-correlation energy due to a particular density $n(\boldsymbol{r})$ could be found by dividing the material into very small volumes with a constant density. Each such volume contributes to the total exchange correlation energy by an amount equal to the exchange correlation energy of an identical volume filled with a homogeneous electron gas, that has the same total density as the original material has in this volume. The local approximation could be reasonable due to the fact that for

the typical densities found in solids, the range of the effects of exchange and correlation is rather short.

2.1.5 Generalized-gradient approximations(GGAs)

The development of various Generalized-gradient approximations (GGAs) comes after the success of LDA since the next logical step was to to make the exchange-correlation contribution of every tiny volume not only depends on the local density in that volume, but also on the density in the neighboring volumes. The use of GGAs can now provide the accuracy required for density functional theory to be widely adopted by the Chemists and Physicists communities. Thus, in GGA there is a functional of the magnitude of the gradient of the density $|\nabla n|$ as well as the value n at each point. The functional could be defined as a generalized form of 2.11:

$$E_{xc}^{GGA} = \int n(\boldsymbol{r})\epsilon_{xc}(n, \nabla n)d^3\boldsymbol{r} \tag{2.12}$$

, where $\epsilon_{xc}(n, \nabla n) = F_{xc}(n, \nabla n)\epsilon_x^{hom}(n)$, F_{xc} is dimensionless, and $\epsilon_x^{hom}(n)$ is the exchange energy of the unpolarized gas. Even though the performance of GGA is slightly better than LDA, there are a few drawbacks. the first one is that There is only one LDA exchange correlation functional, because there is a unique definition for ϵ_{xc}^{hom}. But there is some freedom to incorporate the density gradient, and therefore several versions of GGA exist. the second drawback is that in practice one often fits a candidate GGA-functional with free parameters to a large set of experimental data on atoms and molecules. The best values for these parameters are fixed then, and the functional is ready to be used in solids. Therefore such a GGA-calculation is strictly spoken not an ab initio calculation, as some experimental information is used. Nevertheless, the one used in our calculations is parameter free.

2.1.6 Solving the equations

After using the approach of Kohn-Sham, an infinite set of one-electron equations has been obtained:

$$\left(-\frac{\hbar^2}{2m_e}\hat{\nabla}_m^2 + \frac{e^2}{4\pi\varepsilon_0}\int\frac{\rho(\boldsymbol{r}')}{|\boldsymbol{r}-\boldsymbol{r}'|}d\boldsymbol{r}' + V_{xc} + V_{ext}\right)\phi_m(\boldsymbol{r}) = \epsilon_m\phi_m(\boldsymbol{r}) \tag{2.13}$$

The ϕ_m are mathematical single particle orbitals. Solving in most methods means that we want to find the coefficients C_p^m needed to express ϕ_m in a given basis set ϕ_p^b:

$$\phi_m = \sum_{p=1}^{P} C_p^m \phi_p^b \tag{2.14}$$

The wave functions ϕ_m belong to a function space which has an infinite dimension, P is therefore in principle infinite. Practically, one works with a limited set of basis functions. The use of a limited basis will not be able to describe ϕ_m exactly but finding an appropriate basis can generate a function that is close to the true wave function ϕ_m.

Having chosen a basis (and hence a finite value for P we realize that we can deal with the equations 2.13 as an eigenvalue problem) for a given m, substitute equation 2.14 in 2.13 and left-multiplied with $\langle\phi_i^b|(i=1,\ldots,P)\rangle$, this leads to:

$$\begin{bmatrix} \ldots & \ldots & \ldots \\ \vdots & \langle\phi_i^b|\boldsymbol{H}_{sp}|\phi_i^b\rangle - \varepsilon_m\langle\phi_i^b|\phi_i^b\rangle & \vdots \\ \ldots & \ldots & \ldots \end{bmatrix} = \begin{bmatrix} C_1^m \\ \vdots \\ C_p^m \end{bmatrix} = \begin{bmatrix} 0 \\ \vdots \\ 0 \end{bmatrix} \tag{2.15}$$

Diagonalization of the Hamiltonian matrix will lead to P eigenvalues and P sets of coefficients that express each of the P eigenfunctions in the given basis. When P is larger then the approximated eigenfunction would be close to the real one, but this will lead to the increase of the time consumed in the diagonalization of the matrix in equation 2.15. The basis set that we have used in this work is the linearized augmented plane wave.

2.1.7 The Linearized Augmented plane wave (LAPW) method

The LAPW method is a procedure for solving the Kohn-Sham equations for the ground state density, total energy, and eigenvalues (energy bands) of a many-electron system by introducing a basis set which is especially adapted to the problem. This adaptation is achieved by dividing the unit cell into: (1) non-overlapping atomic spheres (centered at the atomic sites) called muffin tin spheres and (2) an interstitial region as shown in Fig. 2.1. This method uses two different basis sets in the two regions [43]:

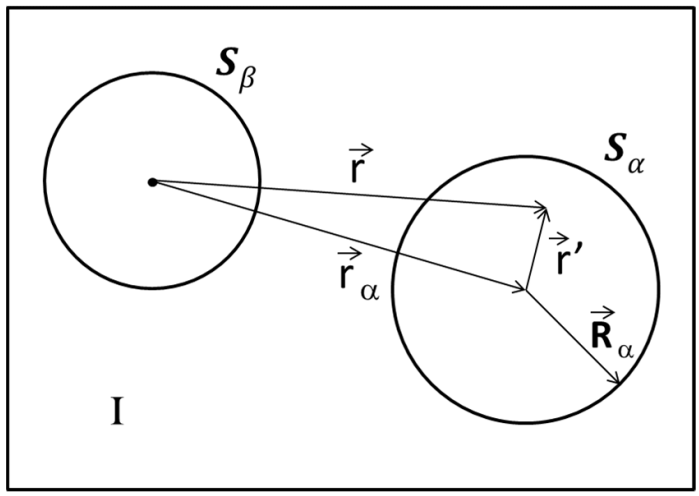

FIGURE 2.1: Division of a unit cell in muffin tin regions and the interstitial region, for a case with two atoms. The block dot is the region of the axis system (which may but not need to coincide with the nucleus of an atom).

1. Inside the atomic sphere (S_α) of radius (R_α) a linear combination of radial functions times spherical harmonics $Y_m^l(\hat{\boldsymbol{r}'})$

is used:

$$\phi_{\boldsymbol{k}}^{\boldsymbol{K}}(\boldsymbol{r}) = \sum_{l,m}(A_{l,m}^{\alpha,\boldsymbol{k}+\boldsymbol{K}} u_l^{\alpha}(r', E_{1,l}^{\alpha}) + B_{l,m}^{\alpha,\boldsymbol{k}+\boldsymbol{K}} \dot{u}_l^{\alpha}(\boldsymbol{r'}, E_{1,l}^{\alpha}))Y_m^l(\hat{\boldsymbol{r'}}) \quad , \tag{2.16}$$

, where $\boldsymbol{K}$ is a reciprocal lattice vector, $\boldsymbol{k}$ is a vector in the first Brillouin zone, $\boldsymbol{r}$ is the vector position, α labels the different atoms in the unit cell,$A_{l,m}^{\alpha,\boldsymbol{k}+\boldsymbol{K}}$, $B_{l,m}^{\alpha,\boldsymbol{k}+\boldsymbol{K}}$ are undetermined parameters, $\boldsymbol{r'} = \boldsymbol{r} - \boldsymbol{r}_{\alpha}$ is the position inside the sphere given with respect to the center of each sphere, $\hat{\boldsymbol{r'}}$ indicates the angles θ' and φ' which specifying the direction of $\boldsymbol{r'}$ in spherical coordinates, $u_l^{\alpha}(\boldsymbol{r'}, E_{1,l}^{\alpha})$ is the solution to the radial part of the Schrödinger equation for a free atom α with energy $E_{1,l}^{\alpha}$ (chosen normally at the center of the corresponding band), and $\dot{u}_l^{\alpha}(\boldsymbol{r'}, E_{1,l}^{\alpha})$ is the energy derivative of $u_l^{\alpha}(\boldsymbol{r'}, E_{1,l}^{\alpha})$ evaluated at the same energy $E_{1,l}^{\alpha}$.

2. In the interstitial region, a plane wave expansion is used:

$$\phi_{\boldsymbol{k}}^{\boldsymbol{K}} = \frac{1}{\sqrt{V}} e^{i(\boldsymbol{k}+\boldsymbol{K})\boldsymbol{r}} \quad , \tag{2.17}$$

, where V is the volume of the unit cell.

The coefficients $A_{l,m}^{\alpha,\boldsymbol{k}+\boldsymbol{K}}$, $B_{l,m}^{\alpha,\boldsymbol{k}+\boldsymbol{K}}$ which appeared in Equation 2.16 are determined by requiring that the function in the sphere matches the plane wave both in value and in slope (derivative) at the sphere boundary (following basis quantum mechanics). But to do that, it is easier first to expand the plane wave in spherical harmonics around the origin of the sphere of the atom α. $u_l^{\alpha}(\boldsymbol{r'}, E_{1,l}^{\alpha})$ and $\dot{u}_l^{\alpha}(\boldsymbol{r'}, E_{1,l}^{\alpha})$ are obtained by numerical integration of the radial part of the Schrödinger equation on a mesh inside the sphere. The solutions of the Kohn-Sham equations are expanded in this combined basis set of LAPW's according to the linear variational method.

$$\phi_{\boldsymbol{k}}^{n}(\boldsymbol{r}) = \sum_{\boldsymbol{K}} C_{\boldsymbol{K}}^{n,\boldsymbol{k}} \phi_{\boldsymbol{k}}^{\boldsymbol{k}}(\boldsymbol{r}) \quad , \tag{2.18}$$

, where n is the band index. The coefficients $C_{\boldsymbol{K}}^{n,\boldsymbol{k}}$ are determined by the Rayleigh-Ritz variational principle. Note that this basis set

is $\boldsymbol{k}$ dependent: all eigenstates $\phi^n_{\boldsymbol{k}}(\boldsymbol{r})$ that have the same $\boldsymbol{k}$ but a different n will be expressed in the basis set this particular value of $\boldsymbol{k}$. For eigenstates with another $\boldsymbol{k}$, a new basis set using a different $\boldsymbol{k}$ has to be used. In practice we cannot work with an infinite basis set, and we have to limit it somehow. For the LAPW basis set a good quantity to judge the accuracy of the result is the product $R^{min}_{\alpha} K_{max}$ between the smallest muffin tin radius and K_{max} (which is the radius of a sphere centered at the origin in the reciprocal space where all the reciprocal lattice vectors that are inside this sphere are taken into the basis set). In the following sections, we will write it RK_{max} for abbreviation.

2.1.8 LAPW with local orbitals (LAPW+LO)

The orbital that contain electron which is extremely well bound to the nucleus and behave almost exactly as if it were in a free atom is called core state. The core state does not participate directly in the chemical bonding with other atoms. Therefore, it must be located entirely in the muffin tin sphere. Valence States leaks out of the muffin tin sphere as they participate in the chemical bonds. while the valence states are treated by the LAPW as plane waves, the Core states are treated as in free atoms, but subjects to the potential due to the valence states. The low-lying valence states (which lay close to the Fermi level) are called semi-core states.

It frequently happens that states with the same l but a different principal quantum number n are both valence states. In this case, another type of basis set should be added to choose the energy $E^{\alpha}_{1,l}$. It is called a local orbital (LO). A local orbital is defined as:

$$\phi^{lm}_{\alpha,LO}(\boldsymbol{r}) = \begin{cases} 0 & \boldsymbol{r} \notin S_{\alpha} \\ [A^{\alpha,LO}_{lm} u^{\alpha}_{l}(r', E^{\alpha}_{1,l}) & \\ +B^{\alpha,LO}_{lm} \dot{u}^{\alpha}_{l}(r', E^{\alpha}_{1,l}) & \\ +C^{\alpha,LO}_{lm} u^{\alpha}_{l}(r', E^{\alpha}_{2,l})] Y^{l}_{m}(\hat{r'}) & \boldsymbol{r} \in S_{\alpha} \end{cases} \tag{2.19}$$

A local orbital is defined for a particular l and m and for a particular atom α. It is zero in the interstitial region and in the muffin

tin spheres of other atoms, hence its name local orbital. In the muffin tin sphere of atom α, the same $u_l^\alpha(\boldsymbol{r}', E_{1,l}^\alpha)$ and $\dot{u}_l^\alpha(\boldsymbol{r}', E_{1,l}^\alpha)$ as in the LAPW basis set are used, with the linearization energy $E_{1,l}^\alpha$ as suitable value for the highest of the two valence states. The lower valence state (that is much more free-atom-like) is sharply peaked at an energy $E_{2,l}^\alpha$). A single radial function $u_l^\alpha(\boldsymbol{r}', E_{2,l}^\alpha))$ at that same energy will be sufficient to describe it. Local orbitals are not connected to plane waves in the interstitial region; they have hence no $\boldsymbol{k}$ or $\boldsymbol{K}$-dependence. The three coefficients $A_{lm}^{\alpha,LO}$, $B_{lm}^{\alpha,LO}$ and $C_{lm}^{\alpha,LO}$ are determined by requiring that the LO is normalized, and has zero value and zero derivative at the boundary of the muffin tin sphere.

2.1.9 General considerations

In its general form, the LAPW method expands the potential in the following form [43]:

$$V(r) = \begin{cases} \sum_{lm} V_{lm}(r) Y_{lm}(\hat{r}) & \text{inside the sphere} \\ \sum_{G} V_G e^{iGr} & \text{outside the sphere} \end{cases} \tag{2.20}$$

, and the charge densities analogously. Thus, no shape approximations are made, a procedure frequently called a full potential method.

2.1.10 WIEN2k Package

The code that we have used in this work is called WIEN2K [43]. The WIEN2K package consists of several independent programs which are linked together via C-SHELL SCRIPTS. The flow and usage of the different programs is illustrated in Figure 2.2. After creating the structure file (a file with extension .struct), which contains information about the structure of the compound, The calculations are initialized. The initialization consists of running

a series of auxiliary programs, which generates the inputs for the main programs. The initialization can be invoked by the script init-lapw, and consists of running:

1. SETRMT a perl program used to select the proper RMT values.
2. NN using this program a list of the nearest neighbor distances up to a specified limit (defined by a distance factor) is created and thus helps to determine the atomic sphere radii. In addition it is a very useful as additional check of the structure file (equivalency of atoms). At the same time it checks that the muffin tin spheres do not overlap.
3. SGROUP determines the space group of the structure defined in the structure file.
4. SYMMETRY generates from the structure file (the initial file) the space group symmetry operations, determines the point group of the individual atomic sites, generates the lm expansion for the lattice harmonics expansion and determines the local rotational matrices.
5. LSTART generates the free atomic densities and determines how the different orbitals are treated in the band structure calculations (i.e. as core or band states, with or without local orbitals). By inspection (from the output of the file), we can decide if it is necessary to include a set of orbitals as local orbitals.
6. KGEN generates a k-mesh in the irreducible part of the BZ.
7. DSTART generates a starting density for the self-consistency cycle (SCF) by a superposition of atomic densities generated in LSTART.

Then, a self-consistency cycle is initiated and repeated until the convergence criteria (energy convergence, charge convergence or force convergence) are reached. This cycle can be invoked with a script called run-lapw, and consists of the following steps:

1. LAPW0 (potential) generates potential from density.
2. LAPW1 (BANDS) calculates the valence bands (eigenvalues and eigenvectors).
3. LAPW2 (RHO) computes valence charge densities from eigenvectors (wave functions).
4. LCORE computes core states and densities.
5. MIXER mixes input and output densities to guarantee convergence.

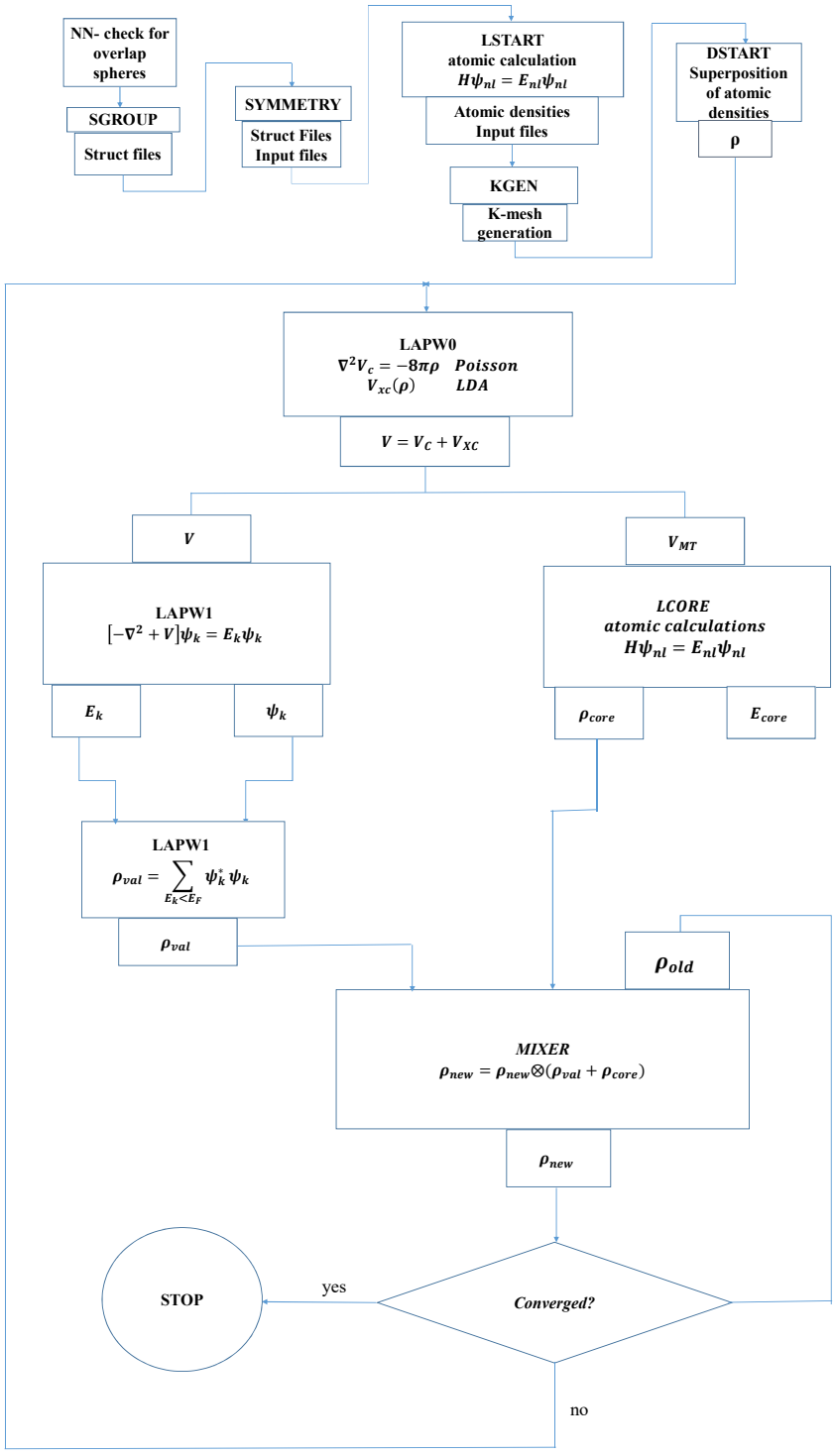

FIGURE 2.2: Program flow in WIEN2k

2.2 Boltzmann theory: The semi-classic equations

The thermoelectric efficiency of a material depends on its electronic and phononic properties. It is characterized by the figure of merit, expressed as:

$$ZT = \frac{s^2\sigma}{\kappa_{el} + \kappa_{ph}}T \quad , \tag{2.21}$$

Where σ and S are the electric conductivity and Seebeck coefficient; κ_{el} and κ_{ph} are the electron and phonon contributions to the total thermal conductivity, respectively and T is the absolute temperature. To obtain good thermoelectric performance, one needs to maximize the power factor $S^2\sigma$ and minimize the thermal conductivity κ.

The parameters in equation 2.21 could be assigned by using the Boltzmann theory [44–47]. When an electric and magnetic field and a thermal gradient are applied, the electric current, $\boldsymbol{j}$ can be written in terms of the conductivity tensors as follows:

$$j_i = \sigma_{ij}E_j + \sigma_{ijk}E_jB_k + \nu_{ij}\nabla_j T + \dots \tag{2.22}$$

The conductivity tensors can be expressed in terms of the group velocity and the inverse mass tensor

$$\sigma_{\alpha\beta}(i,k) = e^3\tau_{i,k}^2 v_\alpha(i,k)v_\beta(i,k) \quad , \tag{2.23}$$

where the group velocity is given by

$$v_\alpha(i,k) = \frac{1}{\hbar}\frac{\partial\varepsilon_{i,k}}{\partial k_\alpha} \tag{2.24}$$

Using the conductivity tensor 2.23, the energy projected conductivity tensors can be defined as:

$$\sigma_{\alpha\beta}(\varepsilon) = \frac{1}{N}\sum_{i,k}\sigma_{\alpha\beta}(i,k)\delta(\varepsilon - \varepsilon_{i,k}) \quad , \tag{2.25}$$

Where N is the number of $K-$points sampled. The transport tensors 2.22 can then be calculated from the conductivity distributions.

$$\sigma_{\alpha\beta}(T;\mu) = \frac{1}{\Omega}\int \sigma_{\alpha\beta}(\varepsilon)[-\frac{\partial f_\mu(T;\varepsilon)}{\partial\varepsilon}]d\varepsilon \tag{2.26}$$

$$\nu_{\alpha\beta}(T;\mu) = \frac{1}{eT\Omega}\int \sigma_{\alpha\beta}(\varepsilon)(\varepsilon-\mu)[-\frac{\partial f_\mu(T;\varepsilon)}{\partial\varepsilon}]d\varepsilon \tag{2.27}$$

$$\kappa^0_{\alpha\beta}(T;\mu) = \frac{1}{e^2T\Omega}\int \sigma_{\alpha\beta}(\varepsilon)(\varepsilon-\mu)^2[-\frac{\partial f_\mu(T;\varepsilon)}{\partial\varepsilon}]d\varepsilon \tag{2.28}$$

where κ^0 is the electronic part of the thermal conductivity. The Seebeck coefficient can be calculated from:

$$S_{ij} = E_i(\nabla_j T)^{-1} = (\sigma^{-1})_{\alpha i}\nu_{\alpha j} \tag{2.29}$$

All the parameters depend on the relaxation time except the Seebeck coefficient, which is independent of τ. Here, the constant relaxation time approximation has been adopted.

2.2.1 BoltzTraP Code

In order to calculate the semi-classic transport coefficients we need to calculate at first the group velocity. The calculation of the group velocity by using the definition in equation 2.24 is numerically difficult to implement. Electronic structure codes usually evaluate the band energies in a numerical mesh for the Brillouin zone sampling; therefore the group velocity must be evaluated as a numerical derivative. This differentiation requires the use

of a computationally costly, very fine grid. To reduce the computational cost, the BoltzTraP program is used [48]. It employs a Fourier expansion of the band energies where the space group is maintained by using star functions.

$$\tilde{\varepsilon}(k) = \sum_{R} C_{Ri} S_R(k), \qquad S_R(k) = \frac{1}{n} \sum_{[\Lambda]} e^{i\boldsymbol{k}\cdot\Lambda\boldsymbol{R}} \quad , \tag{2.30}$$

where $\boldsymbol{R}$ is a direct lattice vector, $[\Lambda]$ are the n point group rotations. The idea is based on using more star functions than the band energies, and constraining the fit so $\tilde{\varepsilon}_i$ are exactly equal to the band-energies, ε_i. Therefore, after obtaining the analytical representation of the band-structure it is then a reasonable procedure to calculate band-structure dependent quantities.

Chapter 3

The structural and electronic properties of GaSe and InSe

3.1 Introduction

In the 1930s, the group $III - VI$ semiconductor layered compounds were discovered [49–51]. They have been characterized by the strong structural anisotropy and nonlinear optical properties [52–61]. A lot of studies have been realized on them from the basic aspects, as their photovoltaic and photoelectronic properties [62–64]. Meanwhile, recently there is a considerable attention to the two dimensional dichalcogenides where the layers are bounded by van der Waals (vdW) forces [65–69] and it is found that the electronic band structure of the bulk case of these compounds change qualitatively as the thickness is reduced down to a few quadruple layers. For example, an indirect to direct gap transition occurs at quadruple layer thicknesses of the Mo and W transition metal dichalcogenides (TMDCs) [70].

In this chapter we present a comprehensive study of the structural and electronic properties for the bulk and quadruple layer ε-polytype of GaSe and InSe using density functional theory.

3.2 The Crystal structure

In the layered materials, each layer has a hexagonal symmetry and it is composed of two planes of metal atoms sandwiched between two chalcogen planes. The bonds inside such a tetralayer are of covalent type with some ionic contribution since the cations are tetrahedrally coordinated (three anions and one cation), while the anions are bounded to three cations. Covalent cation-cation bonds are oriented perpendicular to the layers. This bonds saturate the bonding in the crystal and are responsible for the semiconducting behavior. The layers are stacked together with predominantly van der Waals forces, the distance between the layers is called the van der Waals gap.

Due to the weakness of interlayer bonding, various polytypes exist with different stacking sequences of the layers. The stacking geometry determines the polytype of macroscopic crystal. Most of the structures crystallize in the hexagonal or rhombohedral lattice showing four possible stacking arrangements of the complex layers, leading to four polytypes, named β, ε, γ, and δ. ε, β and δ have hexagonal structure with different number of atoms in the unit cell due to the different stacking while γ has a rhombohedral lattice. The strong covalent bonding within the layer and the weak van der Waals bond between them lead to a strong anisotropy in all the polytypes. Hence the optical and electrical properties, and the thermal conductivity remarkably differ in the directions along the c-axis (perpendicular to the layer planes) and in the plane of the layers.

In the case of GaSe, the most common polytype is the hexagonal [71] $\varepsilon-$GaSe with space group $P\bar{6}m2$ and it is characterized by the two lattice parameters a and c. There are two layers per hexagonal unit cell and two formula units (four atoms) per layer. While for InSe, the most common polytype is $\gamma-$InSe with space group $R\bar{3}m$ with a sequence of three layers in the rhombohedral unit cell [72]. $\gamma-$InSe has a direct band gap of 1.23 eV at room temperature at the Z-point of the rhombohedral Brillouin zone (BZ).

In this work, only the ε-polytype of both GaSe and InSe has been

studied to compare their structural, electrical and thermoelectric properties with the ε-polytype of a new superlattice proposed, $InGaSe_2$. A fragment of the crystal lattice of $\varepsilon-$polytype of GaSe or InSe is shown in fig. 3.1, where the layered atomic arrangement is clearly visible.

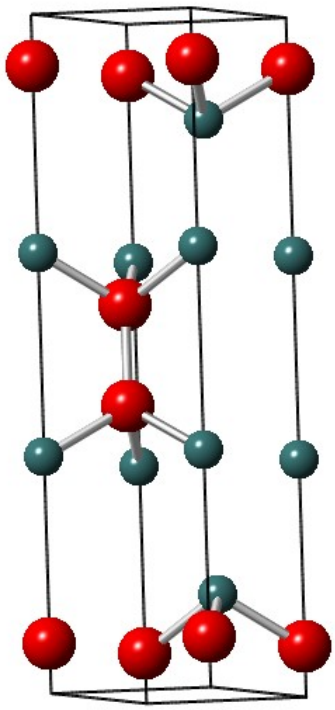

FIGURE 3.1: Unit cell of the hexagonal $\varepsilon-$polytype of GaSe or InSe. The largest spheres (blue) represents the anions (Se) atoms and the smaller ones (red) represents the cations (Ga or In) atoms. Only the bonding between the interlayer atoms is showed to illustrate the layered character of the compounds.

3.3 Computational details

The electronic structure calculations were performed within the framework of the density functional theory by using the full potential linearized augmented plane wave method as implemented in the Wien2k package [43]. Core states are treated within a multi-configuration relativistic Dirac-Fock approach, while valence states are treated in an scalar relativistic approach. The generalized gradient approximation (GGA) with the formalism of Perdew et al. [73] has been used to calculate the exchange correlation energy.

The convergence of the calculations in terms of the size of the plane-wave basis set and the k-points sampling within the irreducible part of the Brillouin zone have been guaranteed by varying the value of R_{MT} K_{max} (where K_{max} the largest K-vector of the plane wave expansion of the wave function and R_{MT} is the atomic sphere radius.). In the following sections, we will write it RK_{max} for abbreviation. G_{max} (where G_{max} is the magnitude of the largest vector in charge density Fourier expansion) and $k-$mesh (the number of $k-points$ in the irreducible wedge of the Brillouin zone), and calculate the total energy as a function of these parameters.

From these calculations the value of RK_{max}, G_{max} and k-mesh at which the total energy is a minimum has been determined. The value of RK_{max} was 12 for the case of GaSe and 13 for the case of InSe. The value of the atomic sphere radius R_{MT} has been chosen to be $2.25, 2.35$ a.u. (atomic units) for In and Se, respectively, in InSe, while for the case of GaSe, it was chosen to be 2.15 $a.u.$ for both Ga and Se. G_{max} was 13 and 14 for GaSe and InSe, respectively. A set of $48k-points$, equivalent to a $14 \times 14 \times 2$ Monkhorst-Pack grid were selected in the unit cell for the two cases. The steps of the structure optimization procedure were:

- firstly, the lattice parameters were taken from experimental studies [74]. For GaSe, the experimental lattice parameters were $a = 0.3759$ nm and $c = 1.5968$ nm, while for InSe $a = 0.3999$ nm and $c = 1.67$ nm.

- Then, the volume has been relaxed towards the minimum of the total energy. From the curves of total energies calculated with the the generalized gradient approximation as a function of the volume, the optimized value of the lattice parameter was taken by using the Birch-Murnagham equation of state.

The Energy-Volume curves were used for the determination of theoretical bulk modulus (B_0) and its pressure derivatives (B'). The last two parameters have been calculated by using the Birch-Murnaghan equation of state. [75].

The electronic band structures of bulk $\varepsilon-$GaSe and $\varepsilon-$InSe have been calculated within the GGA at the theoretical equilibrium lattice constants, the optimized ones, that we have obtained without and with the modified Becke-Johnson correction [76] which allows the calculations of the band gaps with an accuracy similar to very expensive GW calculations [77, 78]. For the quadruple layer structure, the modified Beck-Johnson correction was not used since it is known that the correction doesn't work well for the case of the few layers calculation, and the band structure has been derived using the lattice constant of the optimized bulk structure [43].

3.4 Structural properties

The calculated lattice parameters are given in table 3.1, for $\varepsilon-$GaSe together with some available experimental data and other theoretical results of the lattice parameters and for the case of $\varepsilon-$InSe with the experimental lattice parameters, since there are no more data available .

For $\varepsilon-$GaSe, as can be seen from the table, the calculated lattice parameters in comparison with the theoretical work were found to be similar to that obtained in reference [79], as they have made

TABLE 3.1: Calculated lattice parameters for $\varepsilon-$polytype of GaSe and InSe compared to known experimental data and theoretical results.

Compound	Results	a, b (Å)	c (Å)
GaSe	This work	3.8145	16.2035
	Theory [79]	3.822	16.281
	Theory [80]	3.711	15.67
	Experimental [81]	3.743	15.919
	Experimental [82]	3.753	15.91
InSe	This work	4.1593	17.3649
	Experimental[74]	3.9999	16.6999

the calculation within the DFT theory by using the same approximation for the exchange correlation potential, while the parameters obtained in reference [80] are smaller than our values and the experimental data since they made the calculations using the LDA approximation [40, 83] that usually leads to lower lattice parameters due to the underestimation of the interatomic distance.

For both $\varepsilon-$GaSe and $\varepsilon-$InSe the optimized lattice parameters are larger than the experimental ones. The reason is that these compounds are complicated system for a normal structural optimization procedure, since it includes the interlayer van der Waals interaction that is not taken into account within the DFT. On the other hand, the use of GGA leads to an overestimation of the interatomic distances and hence the lattice parameters. We realized from the table that the lattice parameters for the $\varepsilon-$GaSe is lower than that for the $\varepsilon-$InSe, as it must be, since In is a little bit larger than Ga.

Table 3.2 displays the values of Birch-Murnaghan fitting bulk modulus (B_0) and its pressure derivatives (B') for the bulk and quadruple layer case of GaSe and InSe. As the bulk modulus is a measure of the resistance of the materials to the compressibility. It means that materials with high value of Bulk modulus should be more resistant to be compressed. Hence, from table 3.2 it is expected that for both GaSe and InSe the quadruple layer

TABLE 3.2: Calculated Birch-Murnaghan fitting bulk modulus (B_0) and its pressure derivatives (B′) for the bulk and quadruple layer case of GaSe and InSe. B′ is a dimensionless quantity.

	GaSe		InSe	
	B_0(GPa)	B'	B_0(GPa)	B'
Bulk	53.0987	4.7094	41.4575	4.8207
quadruple layer	26.6447	4.3738	21.6842	5.5696

case should be softer than the bulk case. Also, it can be predicted that GaSe is harder than InSe since the value of the bulk modulus for the bulk and quadruple layer case of GaSe are higher than its counterpart in InSe.

3.5 Electronic properties

3.5.1 Electronic band structure

The investigation of electronic band structure helps to understand the electronic and optical properties of the material. In this section the calculated electronic band structure of the studied materials will be displayed and discussed. Figure 3.2 shows the electronic band structure of the bulk $\varepsilon-$GaSe and $\varepsilon-$InSe. The blue dotted curves represent the band structures that have been calculated by including the modified Becke and Johnson correction (mBJ) while the black curves represent the band structure that has been calculated by using only the GGA with the formalism of Perdew et. al. [73] without including the mBJ correction. The energy is calculated along the high symmetry points, labeled as Γ, M, K, Γ and A.

Fig. 3.2 shows the both valence band maxima and conduction band minima occurs at the center of the Brillouin Zone for $\varepsilon-$GaSe and $\varepsilon-$InSe, indicating that they are direct band gap

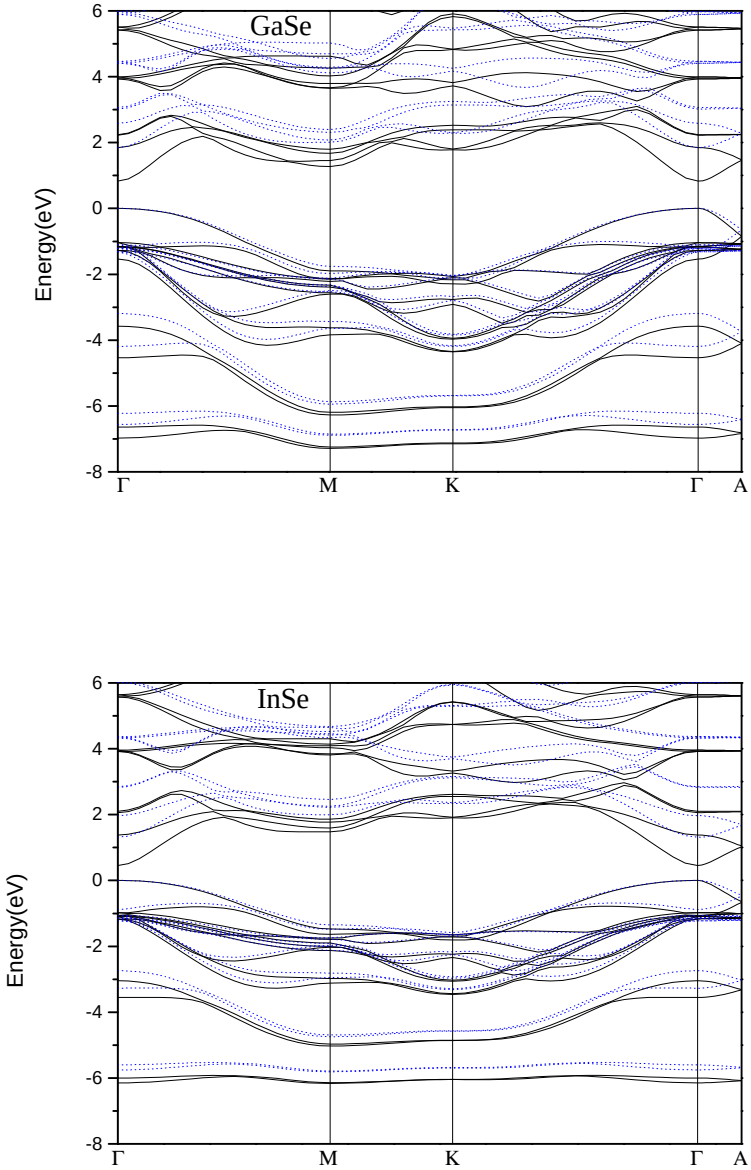

FIGURE 3.2: The calculated band structure for bulk $\varepsilon-$ GaSe and InSe. The dark solid line represents the calculation with GGA. The blue dotted line represents the calculation with GGA+mBJ.

semiconductors. the same results have been obtained in a previous work on $\varepsilon-$GaSe and $\gamma-$InSe [84], but at the $Z-$point of the rhombohedral Brillouin Zone . The band gap value of $\varepsilon-$GaSe and $\varepsilon-$InSe without and with the mBJ correction are shown in Table 3.3. As we can see from Table 3.3, the band gaps calculated with the mBJ are higher than that calculated without it. It is known that DFT underestimates the conduction band energies [85–87], but after using the modified Beck and Johnson correction the minimum of the conduction band has been shifted to higher values leading to an increase of the band gap in both GaSe and InSe, as can be seen from the Fig. 3.2. Hence, the value of the band gap calculated with the mBJ correction is supposed to be closer to the experimental value. Also, the calculated band gap of $\varepsilon-$InSe is lower than that of the $\varepsilon-$GaSe. While the two compounds have a moderate band gap which indicates the thermoelectric performance can be easily optimized within a reasonable doping level. From the figure, it can be noticed also that for the bands located between -7.0 eV and -3 eV, the mBJ correction displaces up the valence bands.

TABLE 3.3: Calculated band gap in eV for the quadruple layer and bulk case of GaSe and InSe

	GaSe			InSe		
	E^{GGA}_{direct}(eV)	$E^{GGA}_{indirect}$(eV)	E^{mBJ}_{direct}(eV)	E^{GGA}_{direct}(eV)	$E^{GGA}_{indirect}$(eV)	E^{mBJ}_{direct}(eV)
Bulk	0.82689		1.85041	0.45096		1.31028
quadruple layer	1.90071	1.80104		1.17843	1.098	

For the quadruple layer case of $\varepsilon-$GaSe and $\varepsilon-$InSe, the calculation has been done using only the GGA. Figure 3.3 displays a comparison between their electronic band structures. Though in the case of a 2D system the dispersion along $\Gamma - A$ of the Brillouin zone has no physical meaning (they are dispersionless since the 2D case is simulating separating the quadruple layers from each other until there is no interaction between them), the curves were plotted along all the high symmetry directions of a 3D Brillouin zone, in order to compare the electronic structure of thin and bulk crystals. As it can be noticed, the band structure of the quadruple layer case is different from the corresponding bulk case. Even though the minimum of the conduction band occurs at Γ, as in the

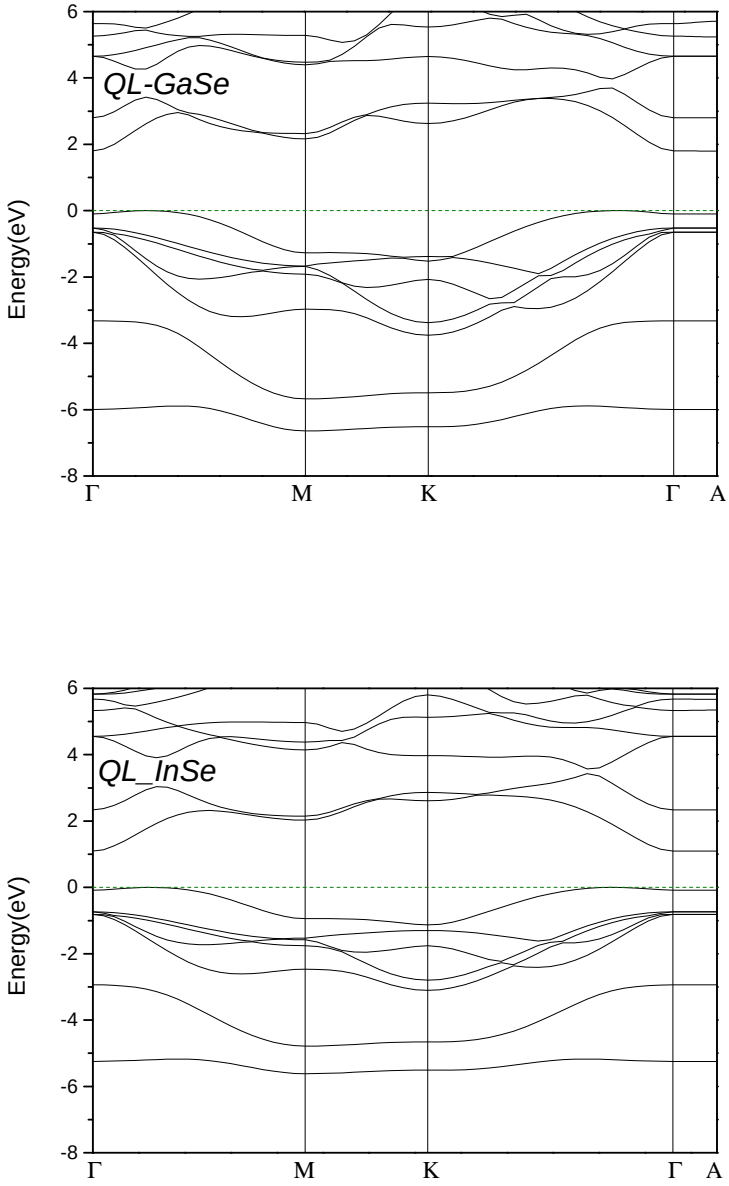

FIGURE 3.3: The calculated band structure for quadruple layer GaSe (upper panel) and InSe (lower panel).

bulk case, the maximum of the valence band is found between K and Γ instead of being at Γ. It means that by moving from the three dimensional case to the two dimensional, the material exhibited a crossover from a direct to an indirect gap semiconductor. Also there is another maximum between Γ and M, the difference between these maxima is about 3×10^{-3} eV. Hence, the valence band is less dispersed than the conduction band. This behavior indicates that the $p-$type doping of this material may be more preferable for good thermoelectric properties than the $n-$type. A similar feature was previously found to exist in bulk InSe under pressure [88].

By looking at Table 3.3, in the quadruple layer case there is a large increase in the band gap value in comparison with the bulk case. This increase could be attributed to the absence of interlayer bond in the quadruple layer case. As the valence band in the quadruple layer case has less dispersion in comparison with the bulk case, the effective mass of the holes in the quadruple layer case is larger than that of the holes in the bulk case. From the values of indirect and direct band gap of the quadruple layer of $\varepsilon-$GaSe and $\varepsilon-$InSe, written down in Table 3.3, we observe that the difference for the two materials is very small. It is about 0.09967 eV for $\varepsilon-$GaSe and 0.08043 eV for $\varepsilon-$InSe. That means that electrons can easily transfer between the two maxima of the valence band with a small amount of energy. The same behavior has been obtained in the previous theoretical study of quadruple layer $\varepsilon-$GaSe [89], as they expected the crossover from direct to indirect gap semiconductor in the 2D sheet limit.

On the other hand, when we compare between the bands in the bulk with that of the quadruple layer, we could see that by moving from the quadruple layer to the bulk the number of band increases due to the splitting of the energy band as a result of the interlayer interaction in the bulk case.

3.5.2 Total and partial density of states

In this section, we present the calculated total density of states (DOS) and partial DOS (PDOS) of bulk and quadruple layer $\varepsilon-$GaSe and $\varepsilon-$InSe. Figures 3.4, 3.5 and 3.6 show the total density of states of $\varepsilon-$GaSe and $\varepsilon-$InSe, the contribution of the Ga atoms to the DOS of $\varepsilon-$GaSe and contribution of the In atoms to the DOS of $\varepsilon-$InSe and, finally, the contribution of the Se atoms to the DOS of $\varepsilon-$GaSe and $\varepsilon-$InSe, respectively. The partial PDOS for each element is a sum of a PDOS over all muffin-tin spheres of the same compound.

The lowest band contribution to the bond is around 7.0 eV below the maximum of the valence band for $\varepsilon-$GaSe while it is around 6.0 eV for $\varepsilon-$InSe. Actually, all the states shown in the figures are $s-p$ cation states hybridized with the p anion states and a very small contribution from s anions. Also, there is a very small contribution of the cation d states. The total density of states $\varepsilon-$InSe is higher than the total density of states of $\varepsilon-$GaSe. The contributions from the orbitals of the cation and anion to the valence and conduction band almost have the same behavior for both of them. The lower valence band is dominated by the main contribution that comes from cation (Ga or In) S states also there are little contributions from Se S, P_z and $P_x + P_y$ states to that band. The valence band at Fermi level has the P character as it is formed mainly from Ga or In and Se P_z and $P_x + P_y$ orbitals, while there is a very small contribution coming from cation (Ga or In) S states. On the other hand, the lower conduction bands are mainly constituted of Ga or In S orbitals hybridized with Ga or In and Se P_z, $P_x + P_y$ states. Also, there is a insignificant contributions coming from Se D states.

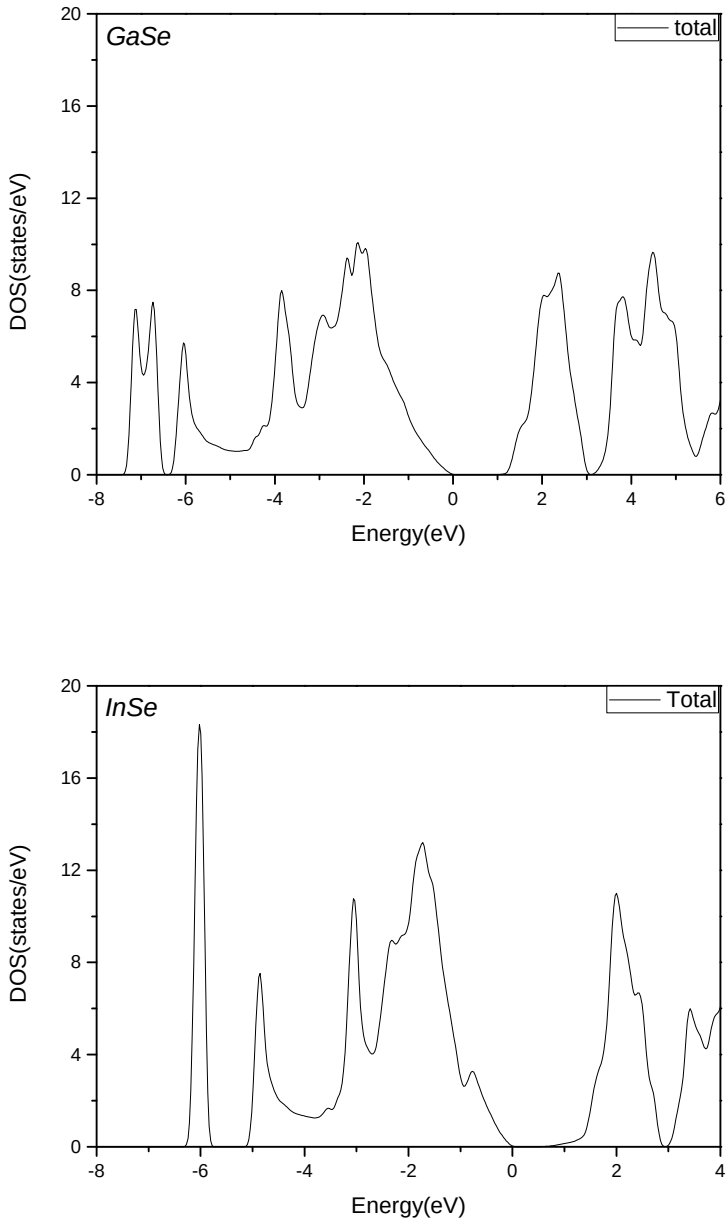

FIGURE 3.4: The calculated total density of states for bulk $\varepsilon-$GaSe (upper panel) and bulk $\varepsilon-$InSe (lower panel).

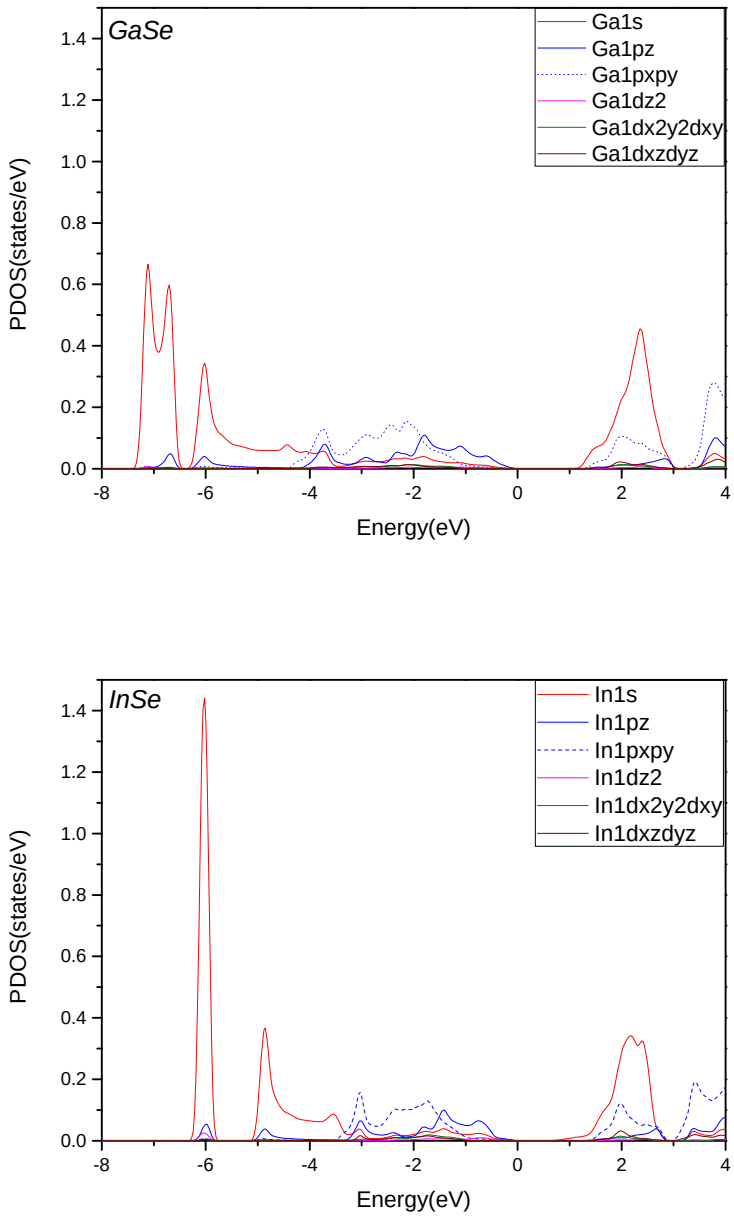

FIGURE 3.5: The partial contribution of Ga atoms (upper panel) and In atoms (lower panel) to the total density of states in bulk $\varepsilon-$GaSe and InSe, respectively

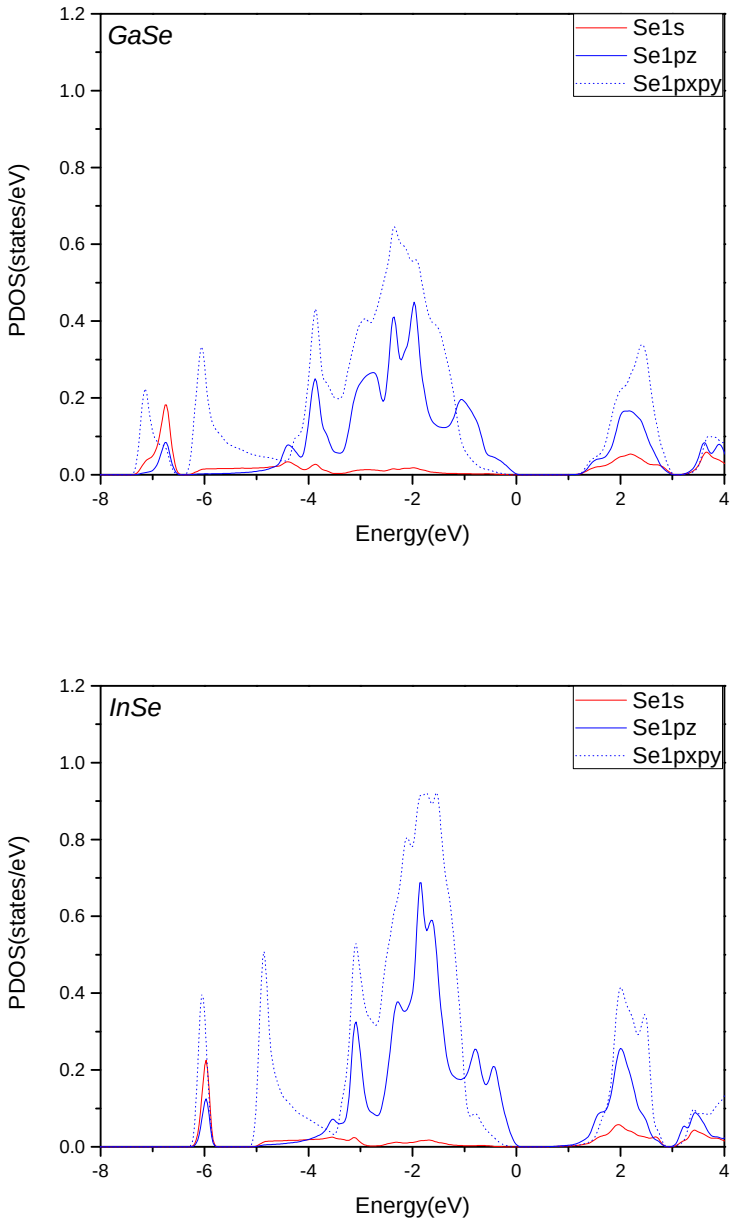

FIGURE 3.6: The partial contribution of Se atom to the total density of states in bulk $\varepsilon-$GaSeand $\varepsilon-$InSe (lower panel)

The quadruple layer total and partial density of states of both GaSe and InSe have been calculated in order to be able to investigate the difference between the two dimensional and three dimensional cases and the results are displayed in figures 3.7, 3.8, and 3.9.

For both GaSe and InSe, even though the contribution of the atomic orbitals was similar to what has been found in the bulk case, the value of the total density of states was smaller in the case of a quadruple layer in comparison with the bulk since in this case the number of atoms is smaller. The most important change was at the maximum in the valence band since in the quadruple layer case there was an abrupt increase in the total density of states at the Fermi level and this could improve the thermoelectric properties of the quadruple layer case. At the same time, in the quadruple layer case the density of states tends to have more defined peaks while for the bulk the curve is smoother.

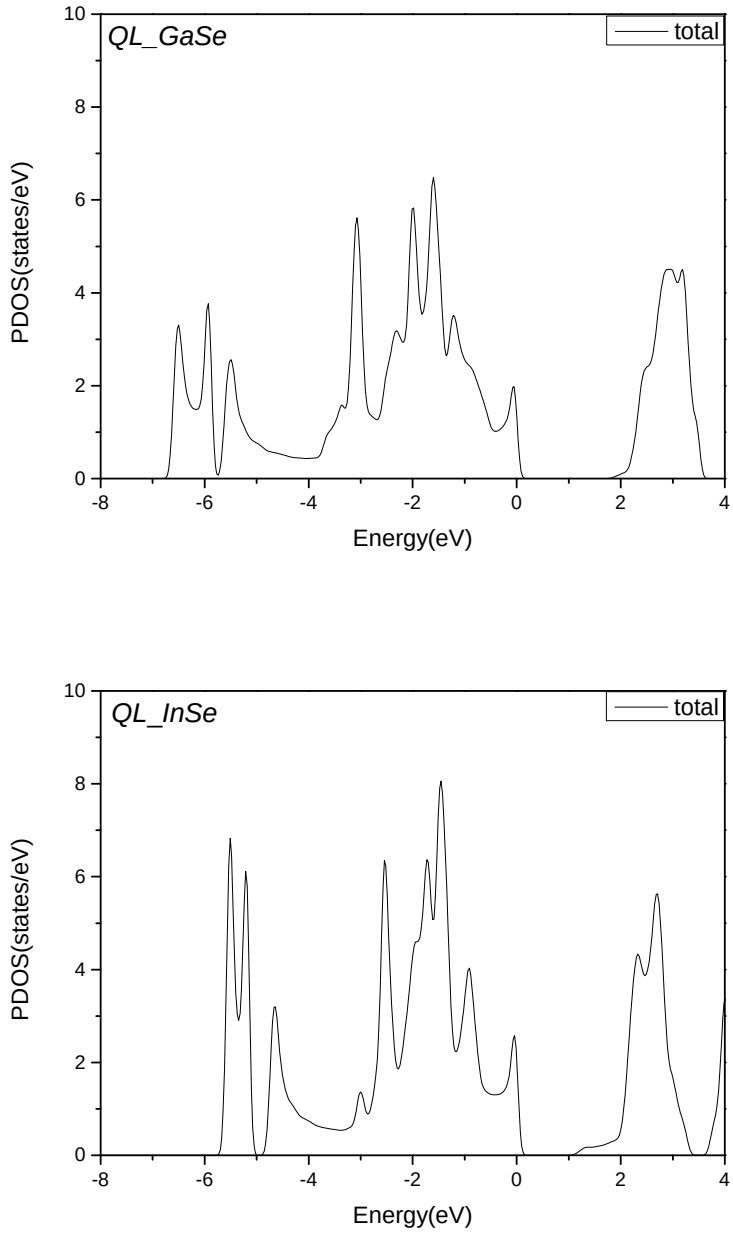

FIGURE 3.7: The calculated total density of states for quadruple layer GaSe (upper panel) and quadruple layer InSe (lower panel)

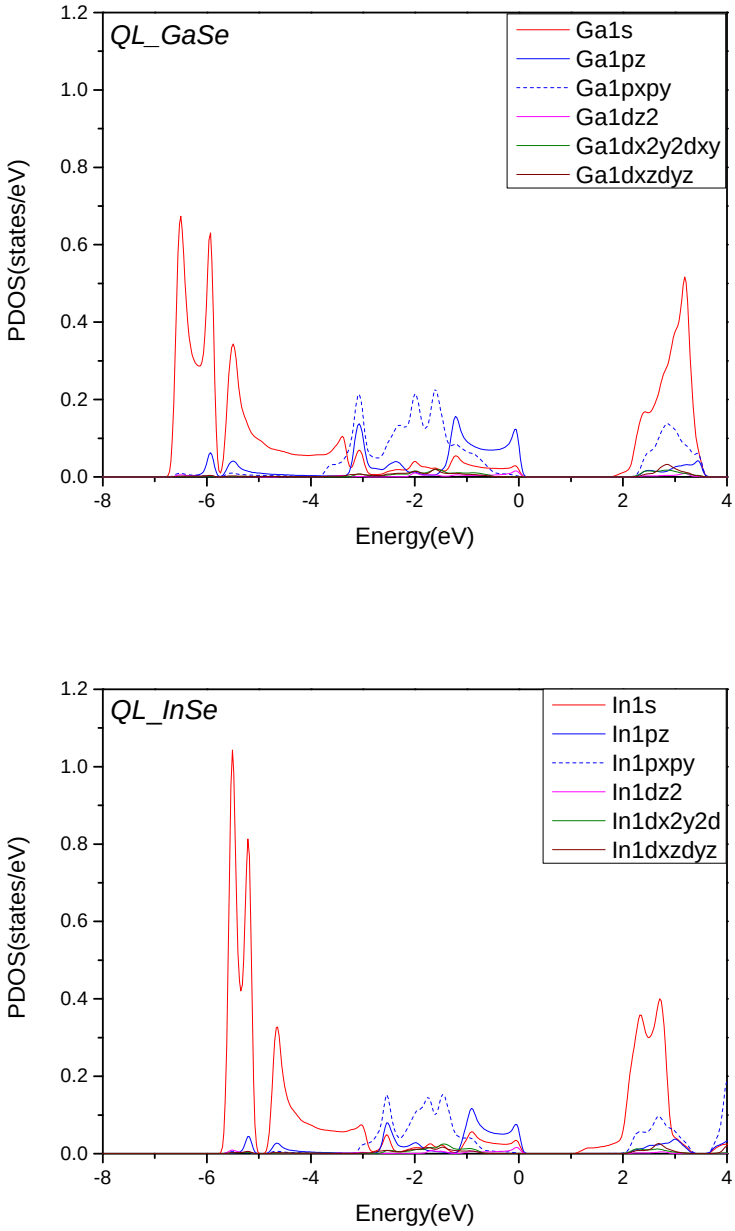

FIGURE 3.8: The partial contribution of Ga and In atom to the total density of states in quadruple layers GaSe (upper panel) and InSe (lower panel), respectively.

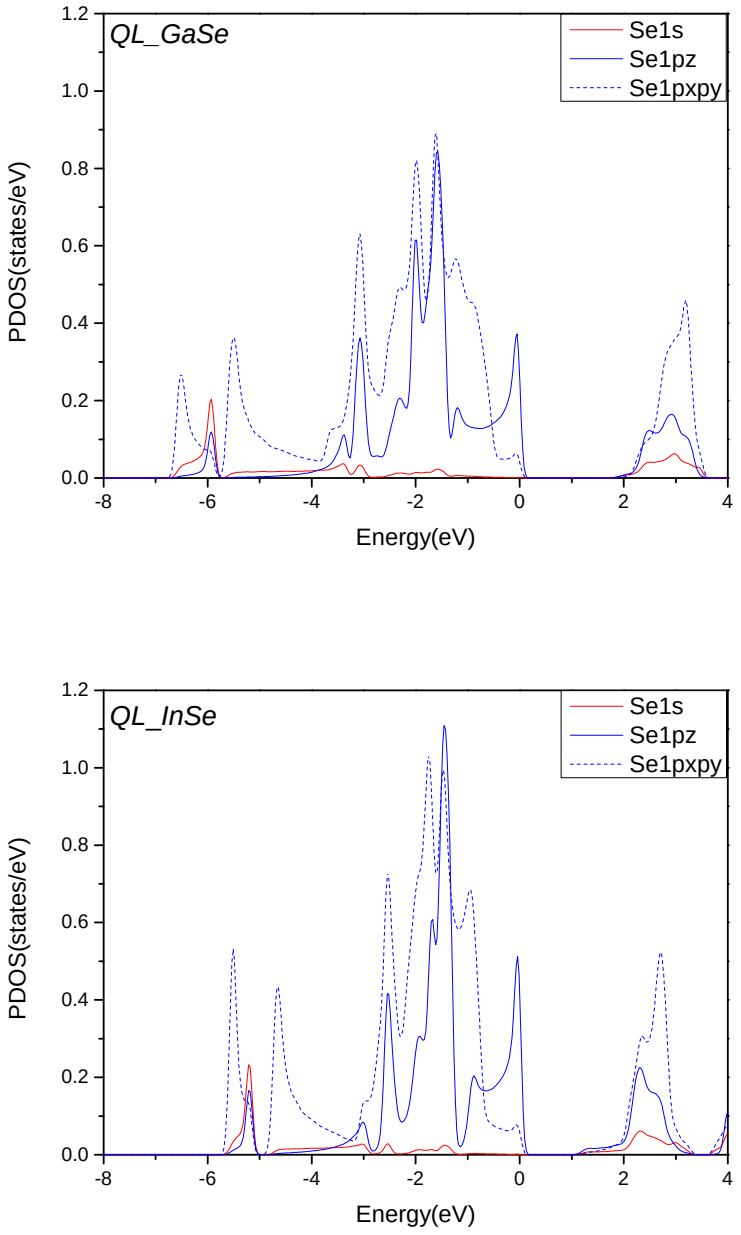

FIGURE 3.9: The partial contribution of Se atom to the total density of states in the quadruple layer of GaSe (upper panel) and InSe (lower panel).

Chapter 4

The structural and electronic properties of $InGaSe_2$

4.1 Crystal structure

The $InGaSe_2$ heterostructure is constructed by simultaneously stacking one layer of GaSe and one layer of InSe. The layers stacking corresponds to the hexagonal $\varepsilon-$polytype with space group $P\bar{6}m2$. In this polytype, the unit cell consists of two layers. In a layer we have the same stacking, independently if we have GaSe or InSe, although the bond distances are different. Each layer has a hexagonal symmetry and is composed of two planes of metal atoms sandwiched between two chalcogen planes. Hence there is one layer where there are two planes of In atoms sandwiched between two planes of Se atoms and the next layer is constituted by two planes of Ga atoms sandwiched between two planes of Se atoms as shown in Fig. 4.1 where four unit cell of $InGaSe_2$ in the xy plane and half layer out of the unit cell in the $z-$direction are drawn.

The unit cell shown in Fig. 4.1 allows us to observe the interatomic bonds. The bonds inside the layer are of covalent type with some ionic contribution. The cations are tetrahedrally coordinated to three anions and one cation while the anions are bounded to three cations. Cation-cation bonds are oriented perpendicular to the layer structure. The two planes of Se atoms in

two adjacent layers are bonded through van der Waals forces and thus, the Se-Se inter-layer distances are larger than the other bond distances. The proposed crystal structure differs from the superlattice proposed by Gashimzade et al. [90], where the stacking of InSe and GaSe are in their bulk-like crystal structure ($\gamma-$InSe/ $\varepsilon-$GaSe). The particular configuration that we have chosen depends on the fact that the symmetries of individual quadruple layers if InSe and GaSe are similar (D_{3h} point group) and such similarity break in the bulk compounds [88]. The In atom has a larger radius than Ga, thus the unit cell of GaSe is smaller than that of InSe. (See Tab 3.1).

Thus, after the optimization of the structural parameters of $InGaSe_2$ we can expect that the layers of GaSe will be tensioned in the plane and thus there will be a compression in the $z-$ direction, while in the case of the InSe layers there will be a compression in the plane and a tension in the $z-$direction.

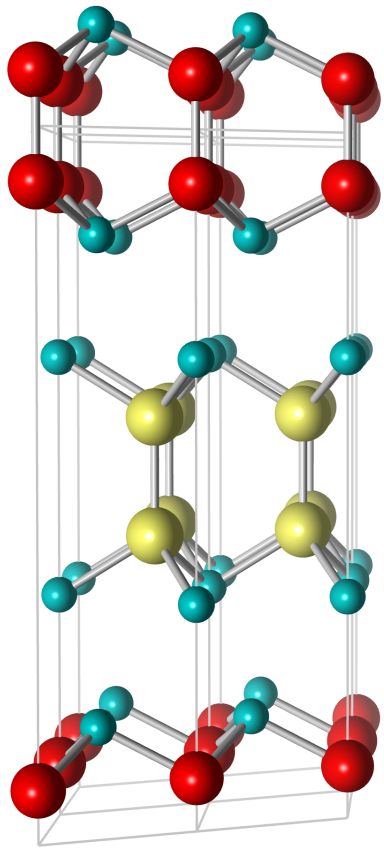

FIGURE 4.1: $InGaSe_2$ supercell with space group $P\bar{6}m2$ showing the stacking of GaSe/InSe. The yellow, red, and Turquoise balls represent indium, gallium, and selenium atoms respectively.

4.2 Computational details

To calculate the electronic band structure, we followed the same procedure as for InSe and GaSe (See chapter 3). The convergence of the total energy in terms of the variational cutoff-parameters has been guaranteed using an appropriate set of parameters. The value of RK_{max} used was 13 while the value of the atomic sphere radius R_{MT} has selected to be 2.2 a.u. for both In and Ga atoms while for Se atom it was 2.3 a.u. The value of G_{max} was 13 and a

set of 60 $k-$points that is equivalent to a $16 \times 16 \times 3$ Monkhorst-Pack grid in the unit cell. For the process of the optimization of the lattice parameters, we started with the average value of the experimental lattice parameters of GaSe and InSe, $a = 3.8795$ and $c = 16.334$ Å. Also, the positions of the atoms inside the unit cell have been optimized by minimizing the forces in the unit cell.

The electronic band structure has been calculated using the optimized lattice constants, like for GaSe and InSe. For bulk $\varepsilon - \mathrm{InGaSe_2}$ the modified Becke-Johnson correction has been included in part of the calculations while for the quadruple layer there was no need not been included.

4.3 Structural properties

The optimized lattice parameters for the $InGaSe_2$ has found to be $a = 3.945$ and $c = 16.61$ Å. The overestimation of the PBE functional to the calculated lattice parameters with respect to experimental measurements [43] has been observed in the pristine compounds GaSe and InSe. Consequently, it could be assumed that, if the superlattice $InGaSe_2$ compound can be synthesized, the experimental value of its lattice parameters should be larger than the values obtained in our calculations. The calculated Birch-Murnaghan fitting bulk modulus (B_0) and its pressure derivatives (B') for the bulk and quadruple layer $\varepsilon-InGaSe_2$ were 48.5627 GPa, 4.8232 and 23.9364, 4.7227 GPa respectively. Since there is much correlation between bulk modulus and hardness of materials, the bulk $InGaSe_2$ should be harder than quadruple layer.

4.4 Electronic properties

4.4.1 Electronic band structure

The upper panel of Fig.4.2 displays the band structure of bulk $\varepsilon - \mathrm{InGaSe_2}$. The blue dotted line and the black solid line represent the calculation with the GGA approximation with including mBJ correction and without it, respectively. Like the pristine materials, InSe and GaSe, the bulk $\varepsilon-\mathrm{InGaSe_2}$ shows a direct semiconductor character Since both the minimum of the conduction band and the maximum of the valence band occurs at the center of the Brillouin zone, Γ. The band gap has decreased in the superlattice $\mathrm{InGaSe_2}$ compared with the band gap in the pristine compounds. The value of the band gap without using the mBJ is $E_g = 0.3814$ eV. The mBJ correction increases the value of the band gap by moving the minimum of the conduction band in the upward direction giving this value for the band gap $E_g^{mBJ} = 1.27233$ eV. It is expected that the experimental value should be closer to this value. While the mBJ correction has almost no effect on the valence band close to the fermi level, its effect on the lower valence band was more clear, since it moves the valence band with energy between -3 and -7 eV in the upward direction.

In the lower panel of Fig.4.2 the electronic band structure of a quadruple layer of $\mathrm{InGaSe_2}$ is presented to show the effect of reducing the dimensionality of this compound on the band structure. The dimensionality reduction was more clear on the valence band than the conduction band. It can be noticed that the minimum of the conduction band still occurs at Γ whereas the maximum of the valence band has moved. Instead of having the maximum at one symmetry point of the Brillouin zone it was between two symmetry points; K and Γ. In the Fig.4.2 there is a blue dotted line at the

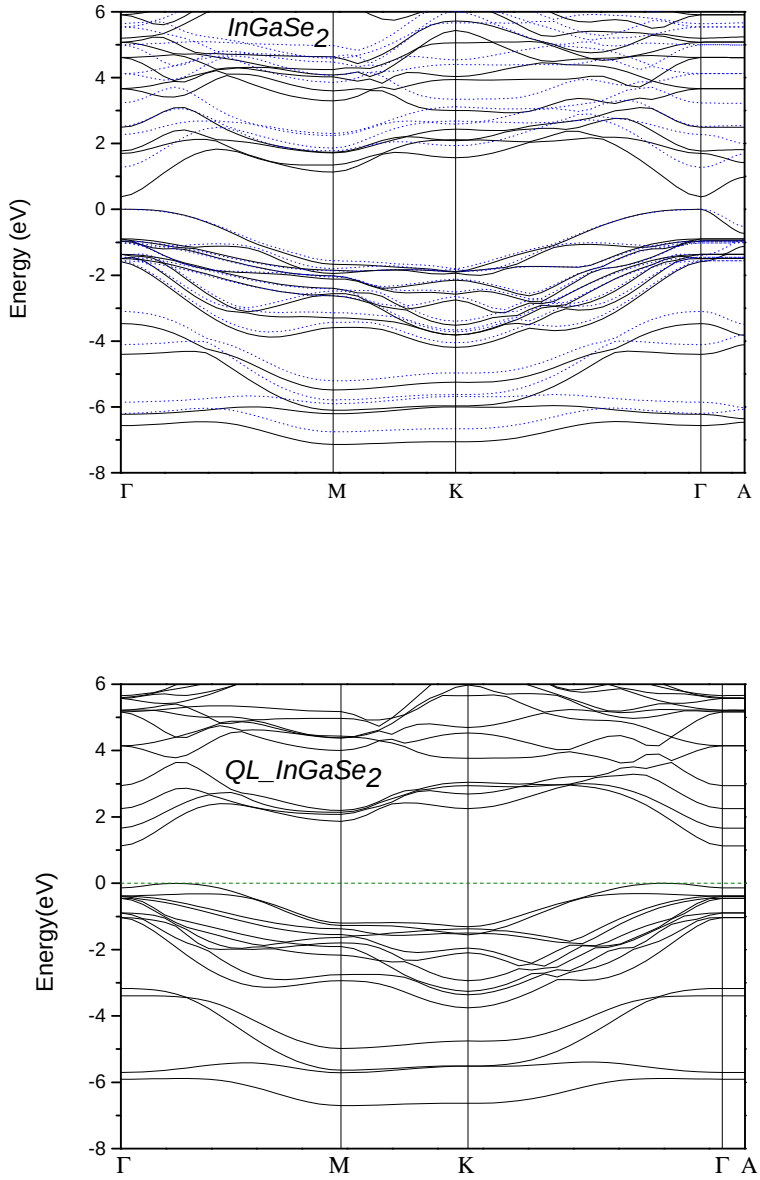

FIGURE 4.2: The calculated band structure for bulk (upper Panel) and quadruple layer (lower panel) $\varepsilon-InGaSe_2$. The dark solid line represents the calculation with GGA. The blue dotted line represents the calculation with GGA+mBJ

Fermi energy to be able to see the maximum of the valence band. It means that the band gap of the quadruple layer $InGaSe_2$ is indirect. The same behavior have been found in the quadruple layer GaSe and InSe. The value of the indirect band gap is $E_g^{indirect} = 1.12457$ eV while the direct band gap is $E_g^{direct} = 1.26685$ eV. Thus there is a small difference between the value of the direct and indirect band gap. At the same time there is another indirect band gap smaller than the direct one between the Γ and M symmetry points, $E_g^{indirect}$ =1.12842 eV. The valence band of the quadruple layer case was flatten and less dispersed in comparison with the conduction band and also with the valence band of the bulk.

4.4.2 Total and partial density of states

The bulk and quadruple layer $\varepsilon-InGaSe_2$ total density of states and the contribution of In, Ga and Se atoms to the total density of states are shown in Fig. 4.3, 4.4, 4.5, and 4.6, respectively. The partial DOS for each element is a sum of a partial DOS over all muffin-tin spheres of the same compound.

In the bulk case, the lowest band contribution to the bond is around -7 eV while for the quadruple layer case it is around -6.5 eV. In the quadruple layer and bulk cases, the contributions of the atomic orbitals to the valence and conduction band are similar. The same that have been illustrated before in the pristine compounds; GaSe and InSe. Also, it can be noticed that in both the lower valence and conduction band, the contribution of the In atoms is larger than the contribution of Ga atoms while their contributions are similar in the higher conduction band.

The lower valence band has the $S-$ character since the most important contribution comes from In and Ga, In spite of $S-$ orbitals, they have also a small contribution from Se, $S-$ and P_x+P_y states. Meanwhile, the valence band at the Fermi level has $P-$ character, The main contribution comes from Se, $P_z$and $P_x + P_y$ states and a little contributions from In and Ga, $P_z$and $P_x + P_y$ whereas the small contributions that comes from $S-$ states of In and Ga cannot be ignored. Finally, the conduction band consists

of a hybridization of In and Ga stares, mainly $S-$ orbitals, and Se, $P_z$and $P_x + P_y$ states.

The most important feature of the density of states in the quadruple layer in comparison with the bulk case is that in the valence band close to the Fermi level there is a sharp increase in the density of states and another defined peak appears there. As well, for the conduction band there is an abrupt increase in the density of states after the minimum of the conduction band which is different from the moderate increase in the bulk case. These features would contribute to improving the thermoelectric properties of the quadruple layer in comparison with the bulk compound that we will see in chapter 5.

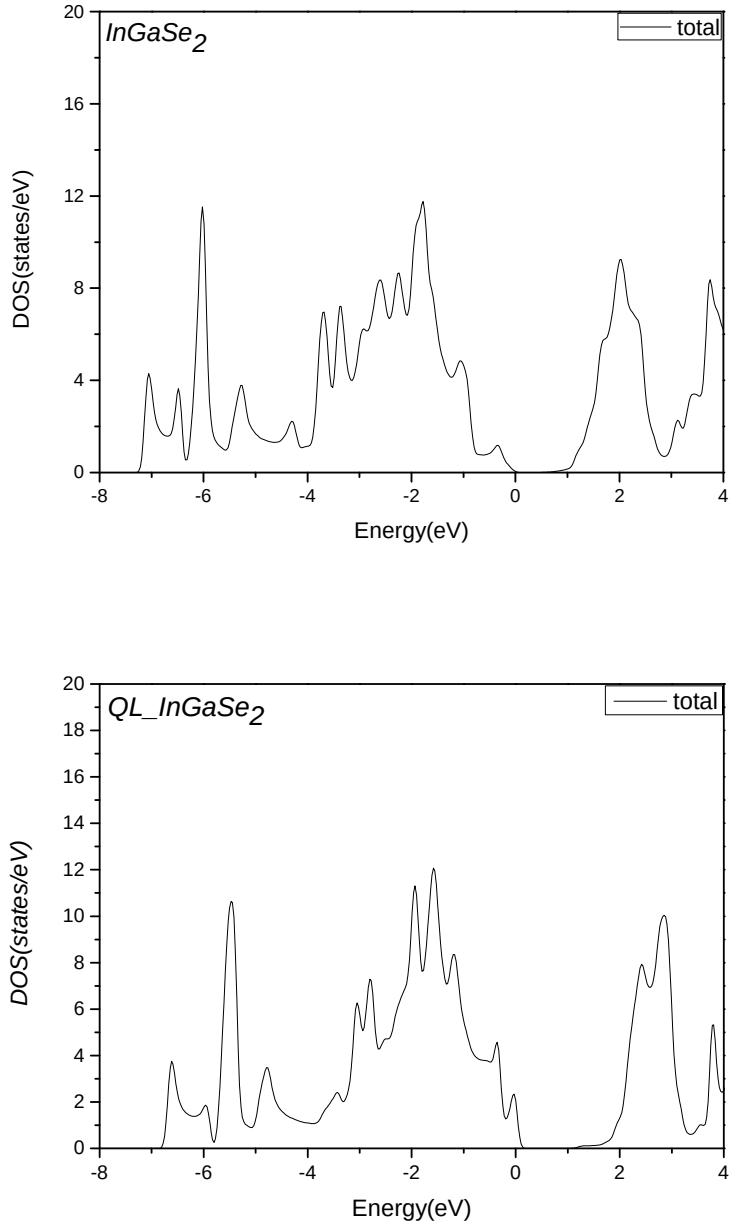

FIGURE 4.3: The calculated total density of states for bulk (upper panel) and quadruple layer (lower panel) $\varepsilon-\mathrm{InGaSe_2}$

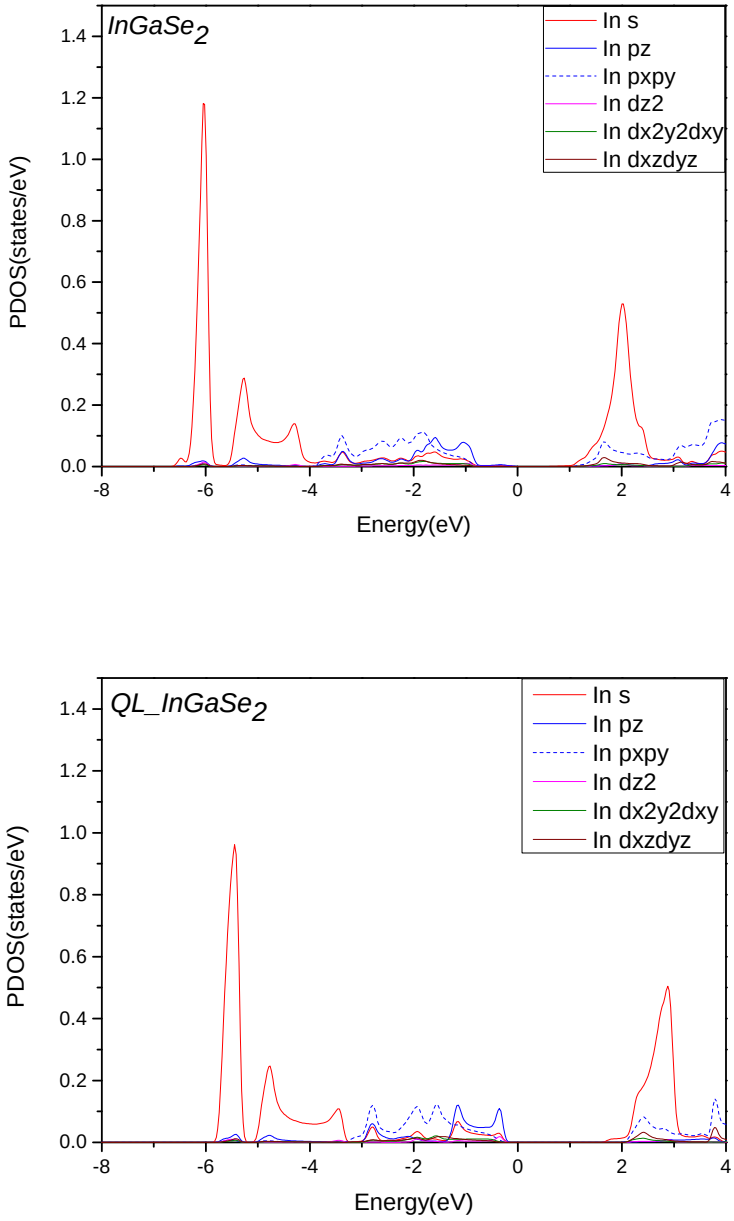

FIGURE 4.4: The partial contribution of In atoms to the total density of states in bulk (upper panel) and quadruple layer (lower panel) $\varepsilon-InGaSe_2$

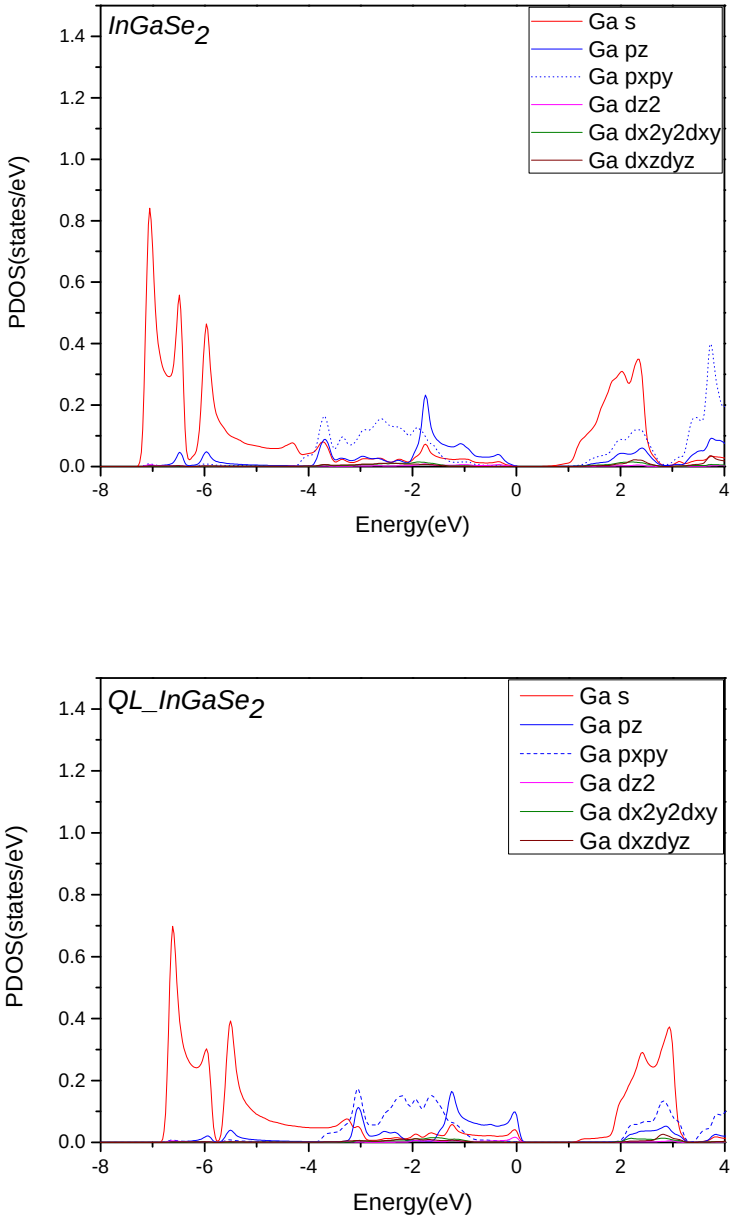

FIGURE 4.5: The partial contribution of Ga atoms to the total density of states in bulk (upper panel) and quadruple layer (lower panel)$\varepsilon-InGaSe_2$

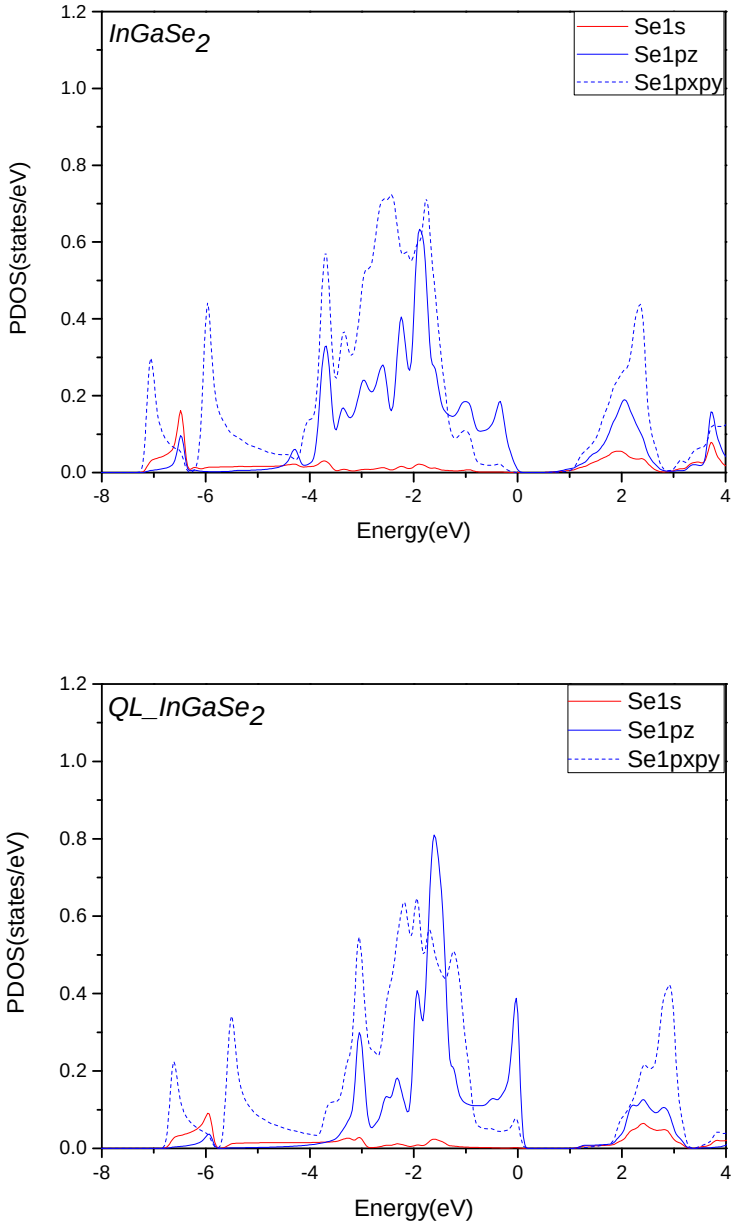

FIGURE 4.6: The partial contribution of Se atoms to the total density of states in bulk (upper panel) and quadruple layer (lower panel)$\varepsilon-InGaSe_2$

Chapter 5

The transport coefficients of GaSe, InSe, and $InGaSe_2$

The power factor PF is closely related with the DOS. Therefore, band gap engineering becomes a very promising tool to obtain thermoelectric properties on demand. According to the Boltzmann transport equation, the thermoelectric transport coefficients can be expressed as a function of the transport distribution function [24, 91], which can be determined by the electronic structure and the electron scattering mechanisms of the materials. Based on the calculations of the band structure of the three materials presented in chapters 3 and 4, the evolution of the thermoelectric properties for the bulk and quadruple layer cases of the $\varepsilon-$GaSe, InSe, and $InGaSe_2$ with respect to the the chemical potential are evaluated with the use of the Boltzmann transport (BT) theory as implemented in the BoltzTraP code. The transport coefficients have been calculated using a dense mesh of 364 $k-$points in the irreducible wedge of the Brillouin zone that is equivalent to a $30 \times 30 \times 6$ Monkhorst-Pack grid.

5.1 The Seebeck coefficient

The voltage difference produced between the two edges of a sample due to an applied temperature gradient between these two points when the electrical current is zero is defined as the Seebeck

coefficient S and it is often referred as thermopower. Actually, if we short circuit the two ends of the sample, a current (electromotive force) will flow through the sample. The response of the materials to any applied temperature gradient can be understood by the behavior of the Seebeck coefficient of the this material. The sign of the Seebeck coefficient with reference to the chemical potential indicates the type of the dominant charge carrier, positive S represents the p-type materials whereas n-type materials have negative S. The chemical potential defines the doping level or carrier concentration in a material, which is very important for enhancing the thermoelectric nature of a material for practical realization. However, we should keep in mind that the magnitude of the charge carrier concentration corresponding to the chemical potential depends on the actual band structures, which are not claimed to be exactly that predicted by single particle DFT calculations. Since it is known that besides the advantage of DFT, it has its limitations [92, 93].

It is well known that the electronic structure near the Fermi energy is significant for the thermoelectric properties *i. e.* when the electronic states of the material under study are extremely dense around the Fermi level; this would play a vital role for the thermoelectric nature of these materials. Thus, we will try to clarify the relation between the electronic structure near the band edges and the results of the Seebeck coefficient.

Within the constant scattering time approximation, the Seebeck coefficient is directly determined by the electronic band structure with no adjustable parameters. The Seebeck coefficients of the bulk $\varepsilon-$polytypes of GaSe, InSe and $InGaSe_2$ vs. the chemical potential at 300 K are presented in Fig. 5.1. It is assumed that $\mu = 0$ corresponds to the middle of the band gap. In the rigid band approximation [94, 95], the band structure is assumed to be unaffected by doping, which only leads to a shift of the chemical potential. For semiconductors, it is a good approximation for the calculation of the transport properties, when the doping level is not too high [96, 97].

The Seebeck coefficient exhibit two pronounced peaks in the vicinity of E_F for n-/p-type regions in all the studied cases. The

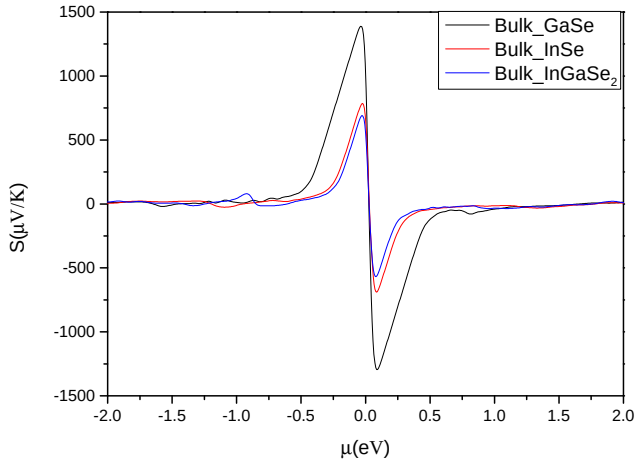

FIGURE 5.1: The Seebeck coefficients of the bulk $\varepsilon-$polytype for GaSe, InSe and $InGaSe_2$ at 300 K.

highest values of the Seebeck coefficient S obtained in the n-/p-type region of the bulk ε polytype of GaSe, InSe and $InGaSe_2$ are listed in Tab.5.1 . From the table we could observe that from all the studied materials, the highest value of the Seebeck coefficient has been achieved for the p-type of GaSe. Even though the values of the Seebeck coefficient obtained in both InSe and $InGaSe_2$ were smaller in comparison with that obtained in the case of GaSe, their values were high in comparison with the typical semiconductors. Usually, the value of the Seebeck coefficient should be larger than 200 μV/K in the efficient thermoelectric materials [98, 99]. To our surprise, no matter p- type or n- type for all the studied materials, the average of S is larger than this value within a reasonable value of the carrier concentration level which indicates higher values of S and may be higher values of $S^2\sigma$ and ZT. We found that our calculated values for the Seebeck coefficient are larger than those found for the Bi_2Te_3 and Bi_2Se_3 systems, as well as for other alloys. For example, at ambient pressure, the measured value for polycrystalline $Sb_{1.5}Bi_{0.5}Te_3$ is reported to be 212 μV/K [100], while a value of 287 μV/°C at 54 °C was reported for a 9.8μm thick Bi_2T_3 thin film[101]. Also from the DFT calculations, using the van der Waals corrections, Luo et al.[102] report a value of S =300μV/K for Bi_2Te_3 while for Bi_2Se_3 they found a

value of S =600μV/K.

TABLE 5.1: The highest values of the Seebeck coefficient S obtained in the n-/p-type region of the bulk $\varepsilon-$polytype of GaSe, InSe and $InGaSe_2$ at 300 K.

	Bulk GaSe		Bulk InSe		Bulk $InGaSe_2$	
	p-type	n-type	p-type	n-type	p-type	n-type
S (μV/K)	1388	-1294	785	-689	691	-567

Furthermore, the maximum value of the Seebeck coefficient for all the studied materials has been obtained at the same chemical potential in the n-type region while for the p-type region there was a small difference between the values of the chemical potential at which the maximum was obtained. When we compare between the Seebeck coefficients in n-type and p-type regions, It can be noticed that for all the materials studied here the Seebeck coefficient was higher in the p-type region.

The range where the materials exhibit good values for the Seebeck coefficient was different in each case as it was wider in the case of GaSe than for both InSe and $InGaSe_2$. The range was $[-0.55, 0.55]$ for GaSe and $[-0.35, 0.35]$ for InSe and $InGaSe_2$. Beyond these points the Seebeck coefficient decreases.

The Seebeck coefficients of the quadruple layer $\varepsilon-$polytype of GaSe, InSe and $InGaSe_2$ materials vs chemical potential at 300 K are presented in Fig. 5.2. We can see how, for the case of quadruple layer GaSe and $InGaSe_2$ there was a discontinuity in the behavior of the Seebeck coefficient, which could be attributed to the accuracy of the calculations. In the study of the thermoelectric properties of the fully hydrogenated graphene, a similar behavior has been obtained for the calculated Seebeck coefficients at 300 K [103]. Also, We noticed that for $InGaSe_2$, outside the region where the Seebeck coefficient exhibits good values, there is a fluctuation in its value as a function of the chemical potential instead of the smooth curves obtained in the other cases.

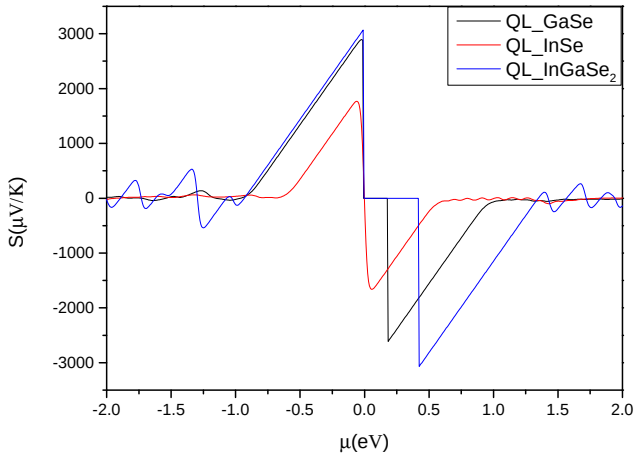

FIGURE 5.2: The Seebeck coefficients of the quadruple layer for GaSe, InSe and $InGaSe_2$ at 300 K

TABLE 5.2: The highest values of the Seebeck coefficient S obtained in the n-/p-type region of the quadruple layer GaSe, InSe and $InGaSe_2$ at 300 K.

	QL GaSe		QL InSe		QL $InGaSe_2$	
	p-type	n-type	p-type	n-type	p-type	n-type
S (μV/K)	2893	-2611	1765	-1662	3069	-3067

In Tab. 5.2, the highest values of the Seebeck coefficient in the n-/p- type region for the quadruple layer case of all the studied materials are recorded. We noticed from the table that the p-type of the quadruple layer $InGaSe_2$ exhibits the highest values of the Seebeck coefficient. For all the studied cases, the maximum value of the Seebeck coefficient was higher in the p-type than in than n-type region, similar to the results obtained in the Bulk case. That indicates the prominence of the p-type on n-type doping in these materials. The range where the quadruple layer exhibit high values for the Seebeck coefficient is wider in the quadruple layer case than in the bulk case.

In comparison with the bulk case, there was a large enhancement in the values of the Seebeck coefficient for the quadruple layer case in all the studied materials. The increase of the Seebeck coefficient for the quadruple layer could be attributed to the following reasons:

1. The strong quantum confinement effect which makes S^2 to increase linearly with decreasing the thickness [35]. This is based on the theoretical prediction of Hicks and Dresselhaus in 1993 that the electronic properties could be enhanced by putting thermoelectric materials in superlattice structures with insulating barrier layers and that the improvement is largest for the shortest period superlattices.

2. The enhancement in the Seebeck coefficient of the quadruple layers can also be explained with the Mahan-Sofo theory [24], which suggests that a local increase in the total density of states over a narrow energy range around the Fermi level can give rise to a high S [104, 105]. In other words, the increase of S could be due to the very higher value of the DOS of the quadruple layer near the Fermi level compared to that of the bulk, which comes from the increase in the contribution of P_z states of both the cation and anion to the DOS near the Fermi level in the quadruple layer case. (see Figs. 3.4, 3.7, 4.3.)

3. The band structure of the studied materials in both the bulk and quadruple layer (see Figs. 3.2, 3.3, 4.2). In the case

of the quadruple layers, the band structure presents more dispersion in the valence band around its maximum value as compared to the bulk. It means that the effective mass of the holes in the quadruple layer case is higher than its corresponding value for the bulk case. If we refer to the relationship between the Seebeck coefficient and the effective mass for the metal[106]:

$$S = \frac{8\pi k_0^2}{3eh^2} m^* T \left(\frac{\pi}{3n}\right)^{2/3}, \tag{5.1}$$

where h, n, e and m^* are Planck's constant, carrier concentration, electronic charge and the effective mass of the carriers, respectively. Even though our materials are semiconductors, we can use this relation 5.1, fully valid for metals, to understand our results in a qualitative way. From this relation we can see that there is a direct relationship between the Seebeck coefficient and effective mass of the carriers. As we have stated that the effective mass of the holes in the quadruple layer case is higher than that in bulk, we should expect that the value of the Seebeck coefficient be larger for the quadruple layer case, which agrees with the results that we have obtained for the Seebeck coefficient which is shown in Fig.5.2.

5.2 Electrical conductivity

The electrical conductivity in metals originates from the motion of the electrons in the conductors while in a semiconductor both holes and electrons contribute to the electrical conductivity. The charge carriers in the semiconductors are usually formed by thermal activation. Hence, their concentration is temperature dependent, in contrary to the case of metal, where the electron concentration is basically constant. According to the equation:

$$\sigma = ne\mu_n + pe\mu_p \tag{5.2}$$

the temperature dependence of the conductivity σ can be expressed as a function of the mobilities μ_n and μ_p of electrons and holes, respectively, and the charge carrier concentration, n for electrons and p for holes.

Based on the electronic structure, we have calculated the electrical conductivity relative to the relaxation time (σ/τ, called the transport function) as a function of the chemical potential. Within the framework of Boltzmann transport (BT) theory [48], the constant scattering relaxation time (τ) approximation is usually adopted. The validity of this approach has been tested earlier [24, 107–110] and the approximation has succeeded even for systems with highly anisotropic crystal axes [110]. Therefore, we will calculate σ/τ instead of σ since in order to calculate τ, an electron-phonon interaction mechanism, or electron-impurity, must be assumed. At the same time, up to our knowledge, there is no data on the scattering rate τ for bulk or quadruple layer of GaSe, InSe or $InGaSe_2$ materials.

Fig. 5.3 shows the evolution of the electrical conductivity of the bulk $\varepsilon-$polytype of GaSe, InSe and $InGaSe_2$ relative to the relaxation time as a function of the chemical potential at $T = 300$ K. The change in the chemical potential μ is equivalent to the doping or the charge carrier concentration.

For all the materials studied, we have the typical semiconductor behavior, σ/τ is zero when the chemical potential is zero and it starts to increases as carrier concentration increases in both p-type and n-type regions. While in GaSe and $InGaSe_2$ the maximum value of σ/τ has been obtained in the n-type region, for the case of InSe, the highest value of σ/τ has been attained in p-type region. Meanwhile, the overall behavior of σ/τ was similar in all the studied materials in both p- and n-type region.

In the n-type region, at a certain value of the chemical potential σ/τ starts to increase abruptly as the chemical potential increases till it reaches the maximum value and then starts to decrease again. The value of the chemical potential at which σ/τ starts to increase or decrease was different in the different materials.

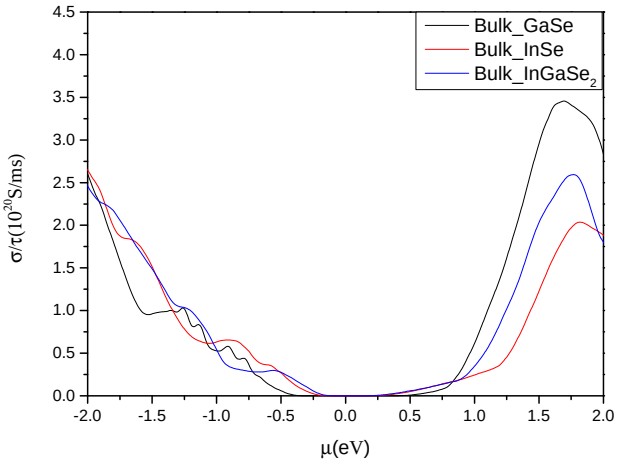

FIGURE 5.3: σ/τ of the bulk $\varepsilon-$polytype for GaSe, InSe and $InGaSe_2$ at 300 K

In the p-type region, although there are some fluctuations in the behavior of σ/τ as a function of the chemical potential, the overall behavior of σ/τ is that it increases as a function of the chemical potential until it reaches a maximum value at a certain value of the chemical potential. The maximum values of σ/τ obtained in p-/n-type region for the bulk case of the three compounds are reported in Tab. 5.3

TABLE 5.3: The highest values of the σ/τ obtained in the n-/p-type region of the bulk $\varepsilon-$polytype of GaSe, InSe and $InGaSe_2$ at 300 K.

	Bulk GaSe		Bulk InSe		Bulk $InGaSe_2$	
	p-type	n-type	p-type	n-type	p-type	n-type
σ/τ $\left(10^{20}\frac{S}{ms}\right)$	2.58	3.45	2.63	2.03	2.45	2.59

The evolution of the σ/τ as a function of the chemical potential at $T = 300$ K is presented in Fig. 5.4 for the quadruple layers of GaSe, InSe and $InGaSe_2$. For all the quadruple layers, the interval at which σ/τ is equal to zero has increased in comparison with their relative bulk cases. In the quadruple layers, the behavior of

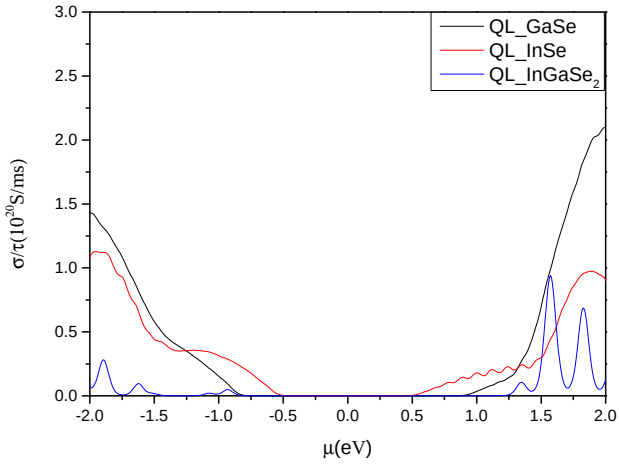

FIGURE 5.4: σ/τ of quadruple layer of GaSe, InSe and $InGaSe_2$ at 300 K.

σ/τ as a function of the chemical potential in the p-type and n-type regions is different in the different materials. For a quadruple layer of GaSe, in n-type region σ/τ increases slowly at the beginning with increasing μ and then abruptly increases untill it reaches its maximum value. The behavior is similar to bulk GaSe but in the present case there is no decrease in σ/τ after reaching its maximum value. In the case of p-type quadruple layers, the fluctuations observed in σ/τ in bulk case disappeared here. The maximum value of σ/τ has been attained for n-type, like in bulk GaSe.

For both n-type and p-type of the InSe quadruple layer, the behavior of σ/τ is similar to the bulk. Its maximum value has also been obtained in the p-type material. For a quadruple layer of $InGaSe_2$, the behavior of σ/τ was completely different from its behavior in the bulk case. Instead of a smooth curve, there were two large peaks in the n-type region and two small peaks in p-type. The values of σ/τ was very small in the p-type case while in the n-type larger values were obtained, although it is still lower than its maximum value in the bulk $InGaSe_2$.

Table 5.4 presents the highest values obtained for σ/τ in p-/n-type region for the quadruple layer case of the three compounds. From Tabs. 5.3 5.4, it can be concluded that the values of σ/τ is larger in the bulk case. This could be attributed to what have been observed before that the value of the DOS for the case of bulk is higher than the DOS for the quadruple layer. (see Figs. 3.4, 3.7, 4.3.)

TABLE 5.4: The highest values of the σ/τ obtained in the n-/p-type region of the quadruple layer GaSe, InSe and $InGaSe_2$ at 300 K.

	QL GaSe		QL InSe		QL $InGaSe_2$	
	p-type	n-type	p-type	n-type	p-type	n-type
σ/τ $\left(10^{20}\frac{S}{ms}\right)$	1.43	2.1	1.13	0.973	0.28	0.94

5.3 Power factors

It is known that the thermoelectric properties of the materials could be improve by enhancing the figure of merit (ZT). The power factor appears in the numerator in the figure of merit relationship $ZT = S^2\sigma T/k$, therefore, improving ZT can occur by maximizing the power factor $PF = S^2\sigma$ or minimizing the thermal conductivity k. Different approaches have been adopted to increase ZT, like doping or lowering the dimensionality of these materials to decrease the thermal conductivity [111, 112]. Also, there is a recent investigation suggesting that the output power, Q, is more important than ZT for the case of unlimited heat source such as solar or waste heat sources [113]. The maximum value of the output power, Q_{max}, includes the power factor ($PF = S^2\sigma$) as $Q_{max} = PF(T_h - T_c)/4L_1$, where T_h and T_c are the hot and cold side temperatures, respectively and L_1 is the length between the hot and cold sides. Hence, this parameter gives an indication of the thermoelectric properties since the higher PF is, the better is the efficiency of the TE device.

Using the existing information on the Seebeck coefficient (S) and the electrical conductivity relative to the relaxation time (σ/τ) presented in the previous sections, one can obtain the power factor relative to the relaxation time ($PF/\tau = S^2\sigma/\tau$). It is clear that the power factor is directly proportional to the Seebeck coefficient square and electrical conductivity. The calculated power factor of the bulk as a function of chemical potential between ± 2 eV at 300 K is illustrated in Fig. 5.5 for the bulk $\varepsilon-$polytypes of GaSe, InSe and $InGaSe_2$. PF/τ were written in units of 10^{14} μW cm^{-1} K^{-2} s^{-1}. At the vicinity of the Fermi level, the power factor exhibits the minimum values. This is attributed to the fact that σ/τ shows the minimum values in the vicinity of the Fermi level (see Fig. 5.3). Hence, the power factor is zero in the same intervals were σ/τ is zero and beyond that the PF/τ increases.

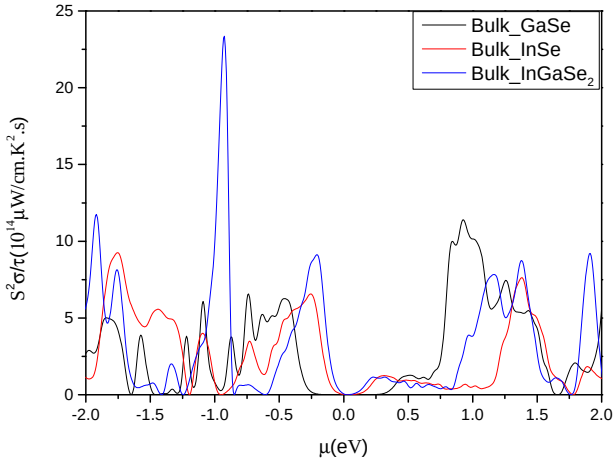

FIGURE 5.5: PF/τ of the bulk $\varepsilon-$polytypes of GaSe, InSe and $InGaSe_2$ at 300 K.

For all the materials studied here, in the n-type region PF/τ starts to increase slowly with the chemical potential. Then, it fluctuates in a small amount until it reaches a certain value of the chemical potential, where PF/τ increases abruptly. After that, there is an oscillation in its value. In this region the material that have shown the maximum value of PF/τ was GaSe. Its maximum value is 11.40×10^{14} μW cm^{-1} K^{-2} s^{-1} at 0.93 eV followed by the value

9.20×10^{14} μW cm^{-1} K^{-2} s^{-1} at 1.90 eV in $InGaSe_2$ and the lowest value, 7.62×10^{14} μW cm^{-1} K^{-2} s^{-1} at 1.40 eV is obtained for InSe.

In the p-type region, for all the compounds, PF/τ starts to increase abruptly at lower values of the chemical potential and then it starts to fluctuate. The behavior of PF/τ in this region shows more fluctuation than in the case of n-type over the same range of the chemical potential. The maximum value of $PF/\tau = 23.35 \times 10^{14}$ μW cm^{-1} K^{-2} s^{-1} at -0.92 eV is obtained for bulk $InGaSe_2$, indicating that the hole contribution is higher in $InGaSe_2$, Next, it comes the value of 9.25×10^{14} μW cm^{-1} K^{-2} s^{-1} at -1.76 eV in InSe and then 6.57×10^{14} μW cm^{-1} K^{-2} s^{-1} at -0.74 eV in GaSe. It means that the maximum value of PF/τ in each material has not been obtained at the same value of the chemical potential. Consequently, from the three investigated bulk cases, the highest value of PF/τ has been attained in p-type $InGaSe_2$. Moreover, for bulk GaSe, the highest PF/τ is obtained in the n-type region, while $InGaSe_2$ and InSe have the reversed tendence.

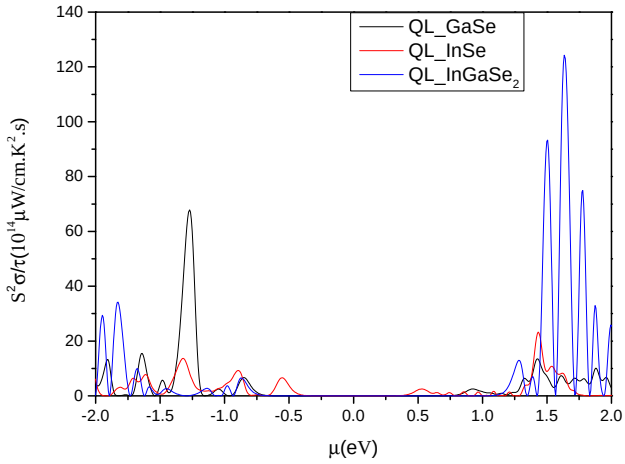

FIGURE 5.6: PF/τ of the quadruple layer for GaSe, InSe and $InGaSe_2$ at 300 K.

The calculated power factor relative to the relaxation time of a quadruple layer of the $\varepsilon-$polytypes of GaSe, InSe and $InGaSe_2$ calculated at 300 K as a function of chemical potential between ± 2 eV is illustrated in Fig.5.6. In the quadruple layers of all the

compounds, there is an improvement in the values obtained for PF/τ in comparison with the bulk cases due to the large values of the Seebeck coefficient in the quadruple layer cases. Even though, the range of the chemical potential where PF/τ equals zero has enlarged. The behavior of PF/τ as a function of the chemical potential was similar in both p-type and n-type regions. First, it increases as a function of the chemical potential till it reaches a certain value and then it starts to decrease again, after that there is a fluctuation in its value.

In the n-type region of $InGaSe_2$, at the 1.63 eV of the chemical potential, the maximum value of PF/τ 124.28×10^{14} μW cm^{-1} K^{-2} s^{-1}. Lower values are obtained for InSe and GaSe: 23.26 and 13.53×10^{14} μW cm^{-1} K^{-2} s^{-1} at 1.4 eV in InSe and GaSe, respectively. Thus, by moving from the 3D to the 2D case, the improvement of PF/τ was magnificent for the $InGaSe_2$ superlattice.

Similar enhancement occurs in p-type, the maximum value has improved in all the studied materials. As the values 67.86 , 34.20 and 13.66×10^{14} μW cm^{-1} K^{-2} have obtained at -1.27, -1.80 and -1.32 eV for PF/τ in GaSe, $InGaSe_2$ and InSe, respectively. Hence, for both GaSe and InSe the best value has been achieved in the p-type region while for $InGaSe_2$ the reversed performance has been found.

5.4 Electronic thermal conductivity

The total thermal conductivity (κ) is the sum of electronic thermal conductivity (κ_e) plus the phonon thermal conductivity (κ_l), *i. e.* $k\kappa = \kappa_e + \kappa_l$, since in metals and semiconductors, the responsible for their thermal conductivity are the electrons and phonon vibrations. Whereas in semiconductors the thermal conductivity is dominated by phonons, in metals this contribution is mainly due to free carriers [114, 115]. BoltzTraP calculates only the electronic part. For simplification, κ is used here to refer to the electronic part of the thermal conductivity instead of κ_e.

The electronic thermal conductivity per relaxation time (κ/τ) in the bulk $\varepsilon-$polytypes of GaSe, InSe and $InGaSe_2$ versus the chemical potential at the temperature of 300 K is depicted in Fig.5.7. When the value of the chemical potential is zero, the thermal conductivity shows its minimum value; it was almost zero and increases as the chemical potential increases.

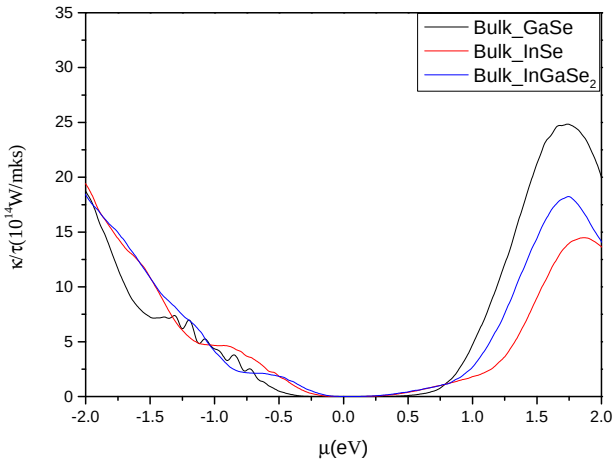

FIGURE 5.7: (κ/τ) of the bulk $\varepsilon-$polytypes for GaSe, InSe and $InGaSe_2$ at 300 K

In the p-type region, the values of κ/τ for all the investigated materials increases as the chemical potential increases. Its peak values obtained at -2 eV were 19.185, 18.487 and 18.241×10^{14} W m^{-1} K^{-1} s^{-1} in InSe, GaSe and $InGaSe_2$, respectively. So the lowest thermal conductivity was the one of $InGaSe_2$ even though the difference between its values in three cases was very small.

In the n-type region, κ/τ firstly increases slowly with the increase of the chemical potential and then after a certain value of the chemical potential there is an abrupt increase. In this region the difference between the κ/τ value from one case to another was larger than in the p-type region. The lowest value of κ/τ has found for InSe in contrary to the p-type region. As the values 24.84, 18.24 and 14.48×10^{14} W m^{-1} K^{-1} s^{-1} has been found in GaSe, $InGaSe_2$ and InSe, respectively. Consequently, the peak

value of κ/τ for $InGaSe_2$ was similar in the two regions while for GaSe and InSe it was smaller the p- and n-type, respectively.

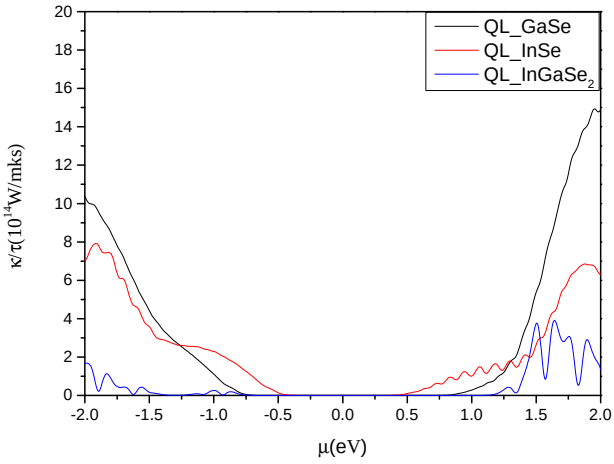

FIGURE 5.8: (κ/τ) of quadruple layer for GaSe,InSe and $InGaSe_2$ at 300 K

Figure 5.8 shows the relation between (κ/τ) and the chemical potential for a quadruple layer of GaSe, InSe and $InGaSe_2$ at 300 K. The behavior of (κ/τ) in a quadruple layer GaSe and InSe is similar to their bulk cases while for the case of $InGaSe_2$ the behavior is different from the bulk case. There is a fluctuation in the value of (κ/τ) as a function of the chemical potential. Overall, the quadruple layer cases exhibit lower values of (κ/τ) in all the materials comparing with the bulk values. $InGaSe_2$ shows the lowest values of (κ/τ) since the largest value of (κ/τ) in the n- and p-type $InGaSe_2$ was 3.9 and 1.68 $\times 10^{14}$ W m^{-1} K^{-1} s^{-1} , respectively. Hence, (κ/τ) in the p-type region of quadruple layer $InGaSe_2$ has lower values.

The maximum value for GaSe was higher in n-type materials, 14.93×10^{14} W m^{-1}k^{-1}s^{-1} than in p-type 10.4×10^{14} W m^{-1} K^{-1} s^{-1}. While for InSe it was higher in p-type 7.9×10^{14} W m^{-1} K^{-1} s^{-1} than n-type 6.85×10^{14} W m^{-1} K^{-1} s^{-1}.

Chapter 6

The transport coefficients at high pressure

In this chapter, the effect of the hydrostatic pressure on the thermoelectric transport coefficients of bulk GaSe, InSe and $InGaSe_2$ $\varepsilon-$polytypes is presented. The calculations have been performed in this order:

- Firstly, the energy structure of the three compounds has been calculated using the WIEN2k code at three different pressures, 0, 10 and 20 GPa. The calculations have been done using the same parameters, RK_{max}, G_{max}, and $k-$points, that have been used before for the different materials and mentioned in the computational details of chapters 3 and 4.
- Then, the the transport coefficients have been calculated using the BoltzTraP code. For these calculations finer $k-$mesh were needed. Hence, a set of 364 $k-$points which is equivalent to $30\times30\times6$ mesh have been used in all the calculations.

6.1 The Seebeck coefficient

Fig.6.1 shows the Seebeck coefficient of $\varepsilon-$GaSe, InSe and $InGaSe_2$ as a function of the chemical potential μ at three different pressures, 0, 10 and 20 GPa. As mentioned before, negative values of the Seebeck coefficient represent $n-$type semiconductors while positive values represent $p-$type. In the vicinity of E_F the Seebeck coefficients exhibit two pronounced peaks for $n-$ and $p-$type materials. From Fig. 6.1 it is noticed that the effect of the pressure on the Seebeck coefficient of the studied materials was different. For InSe, as the pressure increases, the values of the Seebeck coefficient increases and also there is an increase in the range of the chemical potential where the Seebeck coefficient exhibits a good value. It means that the Seebeck coefficient of InSe could be improved by increasing the pressure since the best values of the Seebeck coefficient have been obtained at 20 GPa followed by its values at 10 GPa while its lowest values have been found at 0 GPa. The behavior was different in GaSe and $InGaSe_2$. For both semiconductors, the best values were found at 10 GPa. But when the pressure increases to 20 GPa, the values of the Seebeck coefficient starts to decrease again. For $n-/p-$type $InGaSe_2$ and the $n-$type region of GaSe its values are still better than that calculated at 0 GPa while in the $p-$type region of GaSe its values were lower than that obtained at 0 GPa. A comparison between the maximum values of the Seebeck coefficient obtained at the three different pressures in the $n-$ and $p-$type regions of all the studied cases are written down in Tab.6.1. The values are larger than 200 μV/K, which is required in the efficient thermoelectric materials [98, 99].

TABLE 6.1: The highest values of the Seebeck coefficient S obtained in the $n-/p-$type region of bulk $\varepsilon-$polytypes of GaSe, InSe and $InGaSe_2$ at 0, 10, 20 GPa.

	$\varepsilon-$GaSe		$\varepsilon-$InSe		$\varepsilon-InGaSe_2$	
	$p-$type	$n-$type	$p-$type	$n-$type	$p-$type	$n-$type
$S(\mu V/K)$ at 0 GPa	1388	-1294	785	-689	691	-567
$S(\mu V/K)$ at 10 GPa	1530	-1650	1001	-863	1331	-1329
$S(\mu V/K)$ at 20 GPa	1219	-1330	1395	-1379	1025	-1074

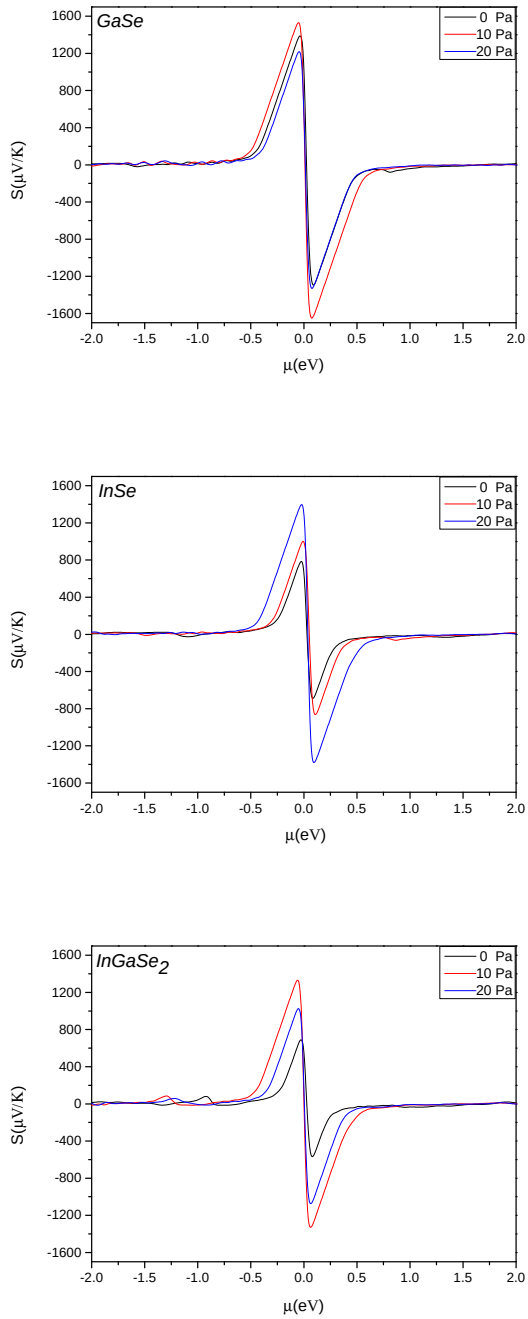

FIGURE 6.1: Calculated Seebeck coefficient as a function of the chemical potential at three different pressures for $\varepsilon-$GaSe, InSe and $InGaSe_2$. The black lines represent the calculated values at 0 GPa, the red lines that calculated at 10 GPa and finally the blue lines represent the calculated values at 20 GPa.

6.2 The electrical conductivity

It was mentioned before that in the output of BoltzTraP the electrical conductivity (σ) is expressed in the form of the ratio (σ/τ), thus without the knowledge of the scattering rate τ the value of the electrical conductivity could not be calculated. The electrical conductivity relative to the relaxation time σ/τ has been calculated as a function of the chemical potential for all the studied materials at the three different pressures and the results are displayed in Fig.6.2.

At zero chemical potential, *i. e.* when the Fermi level is at the middle of the band gap, and close to this value, $\sigma/\tau = 0$ (a typical semiconductor behavior). When the Fermi level moves up or down, the number of charge carriers increases and hence the electrical conductivity starts to increase as a function of the chemical potential. In the $n-$type region, σ/τ increases with the chemical potential till it reaches a maximum and then it starts to decrease again, while in the $p-$type region σ/τ increases first and then there is a fluctuation in its value before it reaches its maximum value.

Also, it can be noticed that the effect of the pressure on the values of σ/τ is direct since its values increase as the pressure increases. Hence, from the results of the Seebeck coefficient and the electrical conductivity it is clear that hydrostatic pressure could be a good tool to improve the thermoelectric properties of the studied materials.

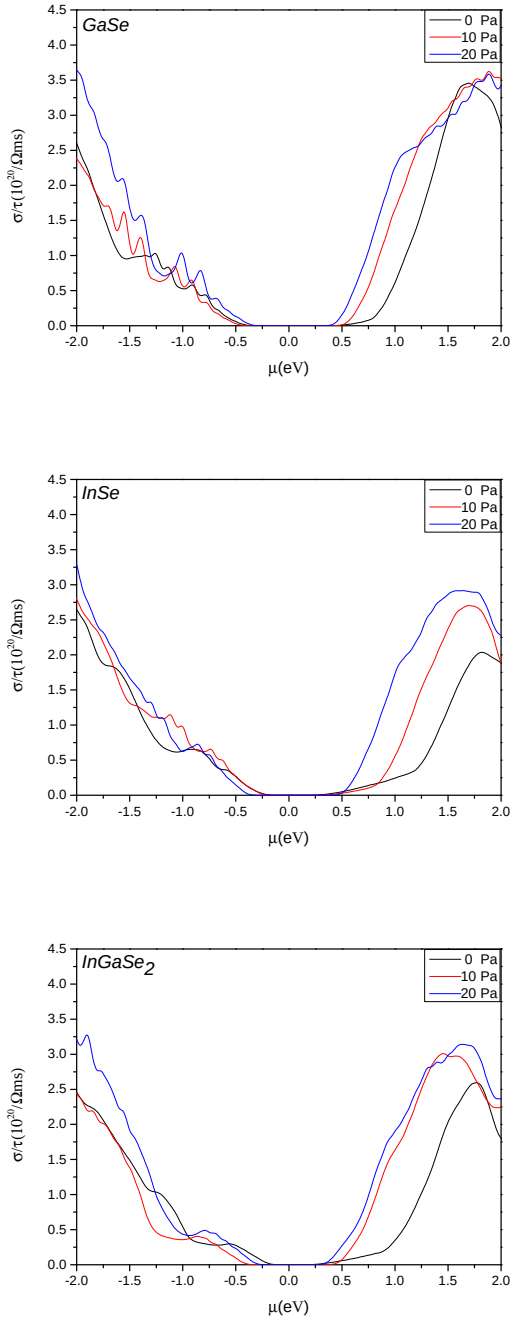

FIGURE 6.2: Calculated σ/τ as a function of the chemical potential at three different pressures for $\varepsilon-$GaSe, InSe and $InGaSe_2$. The black lines represent the calculated values at 0 GPa, The red lines represent the calculated values at 10 GPa and The blue lines represent the calculated values at 20 GPa

6.3 Power factor

As the Seebeck coefficient and the electrical conductivity relative to the relaxation time (σ/τ) have been calculated for GaSe, InSe and $InGaSe_2$ at high pressures, we can obtain the the power factor relative to the relaxation time ($PF/\tau = S^2\sigma/\tau$) at high pressures. The results are shown in Fig. 6.3.

Since the power factor is directly proportional to the Seebeck coefficient square and the electrical conductivity, when the value of $\sigma/\tau = 0$, in particular close to the Fermi energy, the values of PF/τ must be also zero, as it can be observed in Fig.6.3. The general behavior of the effect of the pressure on all the studied cases was the increase of the values of the power factor at small values of the chemical potential, i.e. low doping. The improvement of the values of the PF/τ at a smaller values of the chemical potential was more pronounced in the $n-$type region than in the $p-$type region.

For all the studied materials close to the Fermi level the maximum values of PF/τ were attained at 20 GPa While over all the studied range of the chemical potential, ∓ 2, the pressure at which the maximum of PF/τ is obtained in the different materials was different. Since for InSe the maximum values of PF/τ in both $p-$ and $n-$type was at 20 GPa followed by their values at 10 GPa and the lowest ones obtained at 0 GPa. The same results have been found in GaSe. Meanwhile, the maximum value in $InGaSe_2$ has been obtained at 10 GPa, next comes the value at 20 GPa and finally that calculated at 0 GPa.

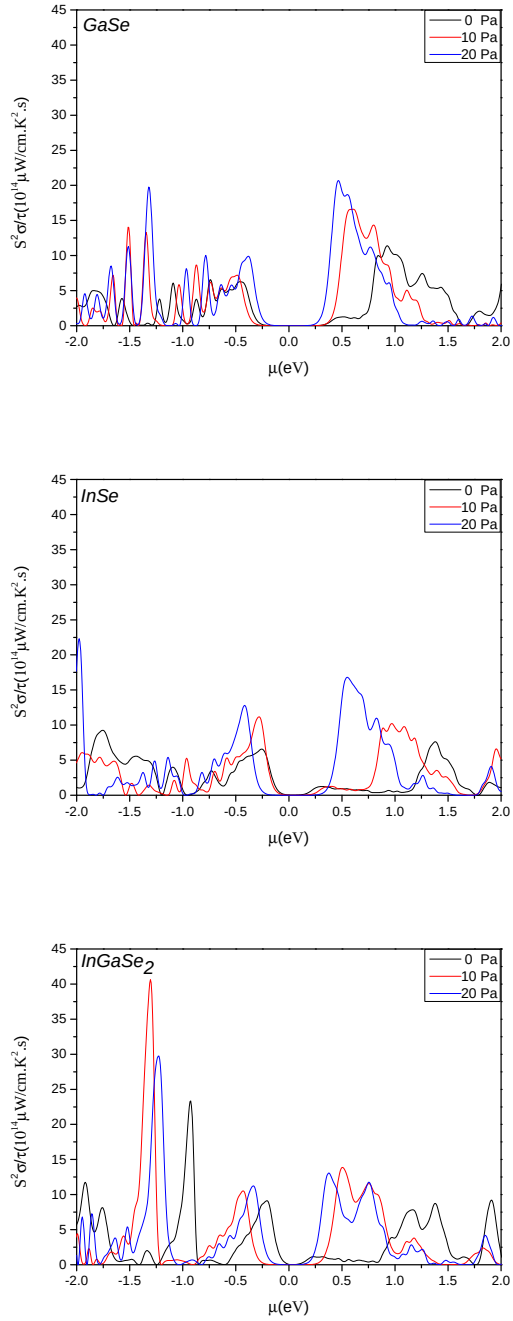

FIGURE 6.3: Calculated PF/τ as a function of the chemical potential at three different pressures for $\varepsilon-$GaSe, InSe and $InGaSe_2$. The black lines represent the calculated values at 0 GPa, The red lines represent the calculated values at 10 GPa and the blue lines the calculated values at 20 GPa

6.4 Electronic thermal conductivity

As mentioned before in the BoltzTraP program only the electronic part of the thermal conductivity could be calculated. Figure 6.4 displays the calculated electronic thermal conductivity per relaxation time (κ/τ) of bulk $\varepsilon-$GaSe, InSe and $InGaSe_2$ versus the chemical potential at three different pressures 0, 10, 20 GPa.

From this figure, it can be observed that the effect of the pressure on the electronic thermal conductivity is positive, that means that the values of the thermal conductivity for all the studied materials increase as the pressure increases. Hence, the lower values of the thermal conductivity are that obtained at 0 GPa. Even though the increase that occurred in the other transport coefficients with the pressure is preferable and makes the pressure to be a good factor to improve the thermoelectric properties of the materials, the increase of the thermal conductivity would lead to a lower value of the "reduced" figure of merit ($ZT/\tau = T\sigma S^2/\kappa\tau$).

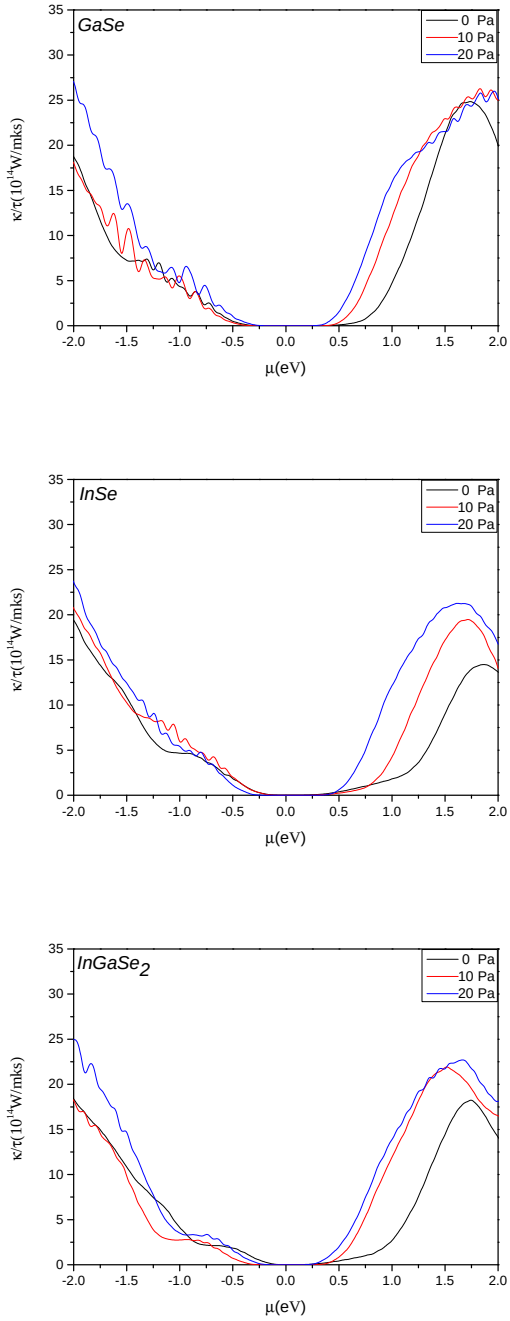

FIGURE 6.4: Calculated κ/τ as a function of the chemical potential at three different pressures for $\varepsilon-$GaSe, InSe and $InGaSe_2$. The black lines represent the calculated values at 0 GPa, The red lines represent the calculated values at 10 GPa and the blue lines the calculated values at 20 GPa.

Chapter 7

Conclusions

The structural, electronic and thermoelectric properties of the $\varepsilon-$polytype of InSe GaSe, and $InGaSe_2$ have been studied at different circumstances. The calculated lattice parameters of both GaSe and InSe have values larger than the values obtained in a previous experimental work. The overestimation of the lattice parameters is one of the shortcut of the generalized gradient approximation in the density functional theory. From this we could conclude that if the heterostructure $InGaSe_2$ could be synthesized, then the experimental lattice parameters should be lower than the values obtained from the values obtained in this study. From the calculated band structure, we noticed that the band gap of the three studied material in the bulk case was direct since both the maximum of the valence band and the minimum of the conduction band occurs at the center of the Brillouin zone, Γ. Also, it has been found that the band gap of $InGaSe_2$ is smaller than the band gap of the pristine compounds GaSe and InSe. In the case of the monolayer the band gap of the materials turned to be indirect due to the changes occur in the top of the valence band. Instead of finding the maximum of the valence band at the Γ point as in the bulk case, the maximum of the valence band has been found between two symmetry points of the Brillouin zone; Γ and K. The contribution of the atomic orbitals to the valence and conduction bands was similar in both the bulk and monolayer case.

Regarding to the thermoelectric properties, we found that in all the studied materials moving from the 3D case to the 2D case,

there is a great enhancement in the values of the Seebeck coefficient. This could be attributed to the quantum confinement effect or the sharp increase in the total density of states at the Fermi level. The contrary have been found for the electrical conductivity since the its values were better in the bulk cases. From the values of the Seebeck coefficient and the electrical conductivity, the power factor values have been calculated. It has been found that in spite of the lower values of the electrical conductivity in the monolayer case its values were lower in the bulk case, the values of the power factor were better in the monolayer case. Further it has been observed that the values of the thermal conductivity were smaller in the monolayer case. It means that these materials could be preferable as a good thermoelectric materials in the low dimension structure than in the bulk.

The effect of the pressure on the Seebeck coefficient values of the studied materials was different from one case to another. For InSe its values increase as the pressure increases therefore the best values have been obtained at 20 GPa while for GaSe and $InGaSe_2$ its values have been improved at 10 GPa but when the pressure increases to 20 GPa the values of the Seebeck coefficient start to decrease again. Furthermore, the pressure has also increased the values of the electrical conductivity. It means that the pressure could be a good factor to improve the power factor of the materials even though it increases at the same time the electronic part of the thermal conductivity.

Chapter 8

Resumen de la Tesis Doctoral

Titulo:
Las Propiedades electrónicas y termoeléctricas del InSe, GaSe e $InGaSe_2$

Los semiconductores del grupo $III - VI$ son materiales laminares que se descubrieron en los años 1930, pero sólo han llamado la atención en las décadas de 1950-1980 debido a su fuerte anisotropía estructural y extraordinarias propiedades ópticas no lineales. En estos materiales cada capa tiene una simetría hexagonal y está compuesta de dos planos de átomos metálicos, arrastrados entre dos planos de un calcogenuro. El enlace dentro de las tetracapas es de tipo covalente con algunas contribuciones iónicas. Las capas se apilan predominantemente a través de fuerzas de van der Waals y la geometría de apilamiento determina el politipo del cristal macroscópico. La mayoría de las estructuras cristalizan en una red hexagonal o romboédrica, mostrando cuatro posibles apilamientos de las capas complejas, dando lugar a cuatro politipos, denominados β, ε, γ, y δ. Los politipos ε, β y δ tienen estructura hexagonal con un número diferente de átomos en la celda unitad mientras que el γ cristaliza en una red romboédrica. Una unión covalente fuerte dentro de la capa y el enlace débil de van der Waals entre las capas conduce a una fuerte anisotropía en todos los politipos. Por tanto, las propiedades ópticas y eléctricas y la conductividad térmica son altamente anisotrópicas, es decir difieren notablemente en las direcciones a lo largo del eje c (perpendicular a los planos de la capa) y paralelas a las capas.

Recientemente el ensamblaje de materiales bidimensionales mediante fuerzas de van der Waals (vdW) ha vuelto a llamar la atención debido a la variedad de propiedades inusuales dependiendo de sus constituyentes y nuevas propiedades físicas. Desde el punto de vista termoeléctrico existe un enfoque bien establecido de que la formación de cristales laminares unidos mediante fuerzas de vdW producen una reducción de la conductividad térmica. Al mismo tiempo gracias a la fabricación exitosa del grafeno, los materiales laminares se han convertido en un objeto de intensa investigación debido a la posibilidad de obtener cristales 2D con un espesor de unos pocos átomos. Se encuentra que la estructura de banda electrónica del caso tridimensional (bulk) de este compuesto cambia cualitativamente a medida que el espesor se reduce a unas pocas monocapas.

Por todas estas razones, el tema central de esta tesis doctoral es la realización del cálculo, mediante técnicas de primeros principios, de las propiedades electrónicas y termoeléctricas del politipo ε del GaSe, InSe la superred $InGaSe_2$, la heterostructura construída por apilado simultáneo de una capa de InSe y una de GaSe, las cuales están ligadas por fuerzas de van der Waals, tanto para el sistema en volumen (bulk) como para la bicapa ($InGaSe_2$).

A continuación se detalla la estructura de la tesis y los aspectos relevantes tratados en cada uno de los Capítulos de la presente Memoria.

En el Capítulo 1 se presenta una breve introducción histórica sobre la termoelectricidad y los materiales termoeléctricos.

En el Capítulo 2 se discuten las teorías y los códigos usados para hacer los cálculos. Este Capítulo ofrece una visión profunda de la teoría del funciónal de la densidad y su implementacion en el código WIEN2k para calcular las propiedades electrónicas y de estructura. También se explica como se implementa la solución semiclásica de las ecuaciones de Boltzmann en el codigo BoltzTraP para calcular los coeficientes termoeléctricos de los materiales.

Los resultados se han estructurado en cuatro Capítulos, del 3 al 6.

En el Capítulo 3 se demuestra una comparacion de las propiedades de estructura, la estructura de banda y la densidad de estado para el sistema en volumen y una monocapa del tipo ε-GaSe e InSe obtenidos del cálculo de primeros principios con el código WIEN2k.

Mientras, en el 4 se presenta la comparación entre las propiedades de estructura y electrónicas para el caso de volumen y una monocapa de la supercelda $InGaSe_2$.

En el Capítulo 5 se muestra como cambian los coeficientes de transportes en función del potencial químico a temperatura ambiente para los tres materiales estudiados; GaSe, InSe y $InGaSe_2$, tanto para el caso en volumen como para el caso de una tetracapa.

Mientras, en el Capítulo 6 se muestra el efecto de la presión sobre las propidades termoeléctricas para el case del sistema en volumen del GaSe, InSe e $InGaSe_2$, ya que los coeficientes de transportes se han calculado a tres presiónes diferentes; es decir a 0, 10, 20 GPa.

Finalmente, en el capitulo 7 se presenta las principales conclusiones del trabajo.

Capítulo 1. Introducción general

El recurso básico utilizado para el suministro de prácticamente todos los recursos al servicio del hombre es la energía eléctrica, con una demanda creciente en los últimos años debido al deterioro ambiental causado por el crecimiento de la población y el desarrollo industrial. Esto produce un enorme consumo de combustibles fósiles. Durante las últimas décadas ha habido un gran interés en la exploración de materiales termoeléctricos eficientes para la generación de energía debido a sus posibles aplicaciones

como fuente de energía limpia y renovable que realizan una conversión directa entre calor y electricidad con muchas características atractivas, tales como vibraciones y ruido, alta fiabilidad y larga vida útil.

El rendimiento de los materiales termoeléctricos puede estimarse por la figura adimensional de mérito $ZT = S^2\sigma T/\kappa$ Donde S ,σ, T son el coeficiente de Seebeck, la conductividad eléctrica y la temperatura absoluta, respectivamente. κ es la conductividad térmica total, que se compone de una contribución electrónica κ_{el} y una contribución fonónica κ_{ph}. Se requiere un alto ZT para una conversión eficiente de energía térmica a eléctrica. Por lo tanto, alto S, alto σ y bajo κ son necesarios.

Capítulo 2. Teoría

Este Capítulo se divide a dos partes:

- La teoría del funciónal de la densidad. La teoría del funciónal de la densidad es una aproximación para la descripción de las propiedades de los metales, semiconductores y aislantes. Los fundamentos de esta teoría fueron proporcionados por Hohenberg y Kohn en 1964, cuando probaron que la densidad de electrones sólo dependía de 3 variables espaciales que contienen en principio toda la información sobre las propiedades del estado fundamental (ground state) de un sistema. Es decir que cualquier propiedad de un sistema de muchas partículas que interactúan puede ser vista como un funciónal de la densidad del estado fundamental $n_0(\boldsymbol{r})$. Sin embargo, ellos no proporcionan ninguna guía para construir los funciónales, y no se conocen funciónales exactos para ningún sistema de más de un electrón. La teoría funciónal de la densidad (DFT) seguiría siendo una curiosidad menor hoy día si no fuera por el Ansatz hecho por Kohn y Sham en 1998, que han proporcionado una manera de hacer útiles funciónales de estado aproximado para sistemas reales de muchos electrones.

El código usado en esta tesis para hacer los calculos de las propiedades de estructura electrónicas se llama WIEN2k. El paquete de programas WIEN2k permite realizar cálculos de estructura electrónica de sólidos utilizando la teoría funcional de densidad (DFT). El paquete WIEN2K consiste de varios programas independientes que están enlazados a través de C-SHELL SCRIPTS.

- La ecuación de transporte de Boltzmann (BTE) describe el comportamiento estadístico de un sistema termodinámico fuera del estado de equilibrio. Según la ecuación de transporte de Boltzmann, los coeficientes de transporte termoeléctrico pueden expresarse en términos de la función de distribución del transporte. Para calcular esta función hay que calcular la Velocidad de grupo; la que se define como el gradiente de la energía en el espacio recíproco. El código usado en la tesis para hacer los calculos de los coeficientes de transporte termoeléctrico es el BoltzTraP. En este código se emplea el desarrollo de Fourier en un punto de la banda de energía para calcular la velocidad del grupo.

Capítulos 3 y 4. Las propiedades estructurales y electrónicas del GaSe, InSe y $InGaSe_2$

En el caso del GaSe, el politipo más común es el hexagonal $\varepsilon-$GaSe con grupo espacial $P\bar{6}m2$ y se caracteriza por dos parámetros de red a y c. Hay dos tetracapas por celda unitaria hexagonal y dos unidades de su fórmula química (cuatro átomos) por tetracapa. Para el InSe, el politipo más común es $\gamma-$InSe con grupo espacial $R\bar{3}m$ con una secuencia de tres tetracapas en la celda unitaria romboédrica. El $\Gamma-$InSe tiene una anchura de banda directa de 1.23 eV a temperatura ambiente en el punto Z de la zona de Brillouin (BZ) romboédrica.

En este trabajo, sólo se ha estudiado el politipo ε del GaSe e InSe para comparar sus propiedades estructurales, eléctricas y

termoeléctricas con el politipo ε de la nueva estructura propuesta $InGaSe_{\mathbf{2}}$.

La celda unitaria de la supercelda del $InGaSe_{\mathbf{2}}$ está compuesta de una capa de GaSe y una capa de InSe. El apilamiento de las capas que se han estudiado en este trabajo corresponde al politipo hexagonal ε, por lo que el grupo espacial es el $P\bar{6}m2$. Cada tetracapa tiene simetría hexagonal y está compuesta por dos planos de átomos metálicos intercalados entre dos planos de calcogenuro. Por lo tanto, en el $InGaSe_2$ hay una tetracapa donde hay dos planos de los átomos de In intercalados entre dos planos de átomos de Se y la siguiente tetracapa está constituída por dos planos de átomos de Ga intercalados entre dos planos de átomos de Se. Los dos planos de átomos de Se en dos tetracapas adyacentes están unidos a través de fuerzas de van der Waals y, por lo tanto, las distancias inter-capa Se-Se son mayores que las otras distancias de enlace.

El átomo de In tiene un radio covalente e ionico mayor que el Ga, por lo que la celda unitaria del GaSe es menor que la del InSe. Así que después de la optimización de los parámetros estructurales de $InGaSe_2$ las capas de GaSe eran tensionadas en el plano y comprimidas en la dirección z, mientras que en el caso del InSe habría una compresión en el plano y una tensión en la dirección z.

Los cálculos de la estructura electrónica se realizaron dentro del marco de la teoría del funcional de la densidad, utilizando el método de ondas planas aumentadas linearizadas de potencial completo implementado en el código de Wien2k. Se ha garantizado la convergencia de los cálculos en función del parámetro interno del programa y también se ha optimizado los parameteros de red hasta obtener el mínimo de energía total. La aproximación del gradiente generalizado (GGA) mediante el formalismo de Perdew et al. ha sido utilizado para calcular la energía de correlación de intercambio (exchange correlation energy). Para mejorar la precisión del cálculo de la anchura de banda (band gap) se ha implementado la corrección de Becke-Johnson modificada. Para el caso de una monocapa no se ha agregado la corrección de Becke-Johnson modificada debido a su posible inestabilidad.

Resultados y discusión

- Los parametros de red optimizados usando La aproximación GGA para el $\varepsilon-$GaSe e InSe han resultado mayores que los valores experimentales.

  La razón es que estos compuestos son un sistema complicado para el procedimiento de optimización estructural, ya que incluye las interacciones entre tetracapas van der Waals que no se tienen en cuenta dentro de la DFT. Y el uso de GGA conduce a la sobreestimación de la distancia interatómica y, por tanto, los parámetros de la red. Tambien se observa que los parámetros de la red para el GaSe son inferiores a los del InSe. Por lo tanto, se podría suponer que si el compuesto $InGaSe_2$ puede ser sintetizado, el valor experimental de esta supercelda debería ser menor que los valores obtenidos en este cálculo.

- En la estructura de bandas, para el caso del sistema en volumen en los tres materiales, tanto los máximos de la banda de valencia como los mínimos de la banda de conducción ocurren en el centro de la zona de Brillouin, el punto Γ. Esto indica que son semiconductores de anchura de banda directa (direct gap). El valor la anchura de banda en la superestructura $InGaSe_2$ es menor que la del GaSe e InSe. Después de usar la corrección de Becke y Johnson modificada (mBJ), el mínimo de la banda de conducción se ha desplazado a valores más altos que conducen a un aumento en el valor de la anchura de bandas en el GaSe e InSe.

  La estructura de bandas del caso de una tetracapa en los dos materiales es diferente de la correspondiente al caso del sistema en volumen. Aunque el mínimo de la banda de conducción se produce en Γ igual que en el caso del sistema en volumen, el máximo de la banda de valencia se encuentra entre K y Γ en lugar de estar en Γ. Esto significa que al pasar del caso tridimensional al bidimensional de los mismos compuestos, los materiales pasan a tener una banda indirecta. La banda de valencia en el caso de una monocapa es más plana, es decir hay menos dispersión, en comparación con la banda de valencia del caso volumétrico.

- En los dos materiales, la contribución de los orbitales atómicos a la densidad total de estado de la banda de conducción y la banda de valencia fue similar tanto para el caso en volumen como para una monocapa.

Capítulo 5. Los coeficientes de transporte del GaSe, InSe, e $InGaSe_2$

El factor de potencia (PF) está relacionado con la densidad de estados, por lo que la denominada ingeniería de la anchura de banda se convierte en una herramienta muy prometedora para obtener propiedades termoeléctricas a la carta. De acuerdo con la ecuación de transporte de Boltzmann, los coeficientes de transporte termoeléctrico pueden expresarse en términos de la función de distribución de transporte que puede determinarse por la estructura electrónica y el mecanismo de dispersión de electrones de los materiales. En este Capítulo se han estudiado el coefeciente de Seebeck, la conductividad eléctrica, el factor de potencia y la conductividad térmica.

Resultados y dicusión

- En la representación del coeficiente Seebeck para los tres materiales estudiados en función del potencial químico a temperatura ambiente se puede ver que el coeficiente Seebeck en la vecindad de E_F exhibe dos picos pronunciados para un semiconductor de tipo $n-/p$, ya que S positivos representan los materiales tipo$-p$ mientras que los de tipo$-n$ tienen S negativos.
  - En el sistema en volumen de todos los casos estudiados se ha obtenido el valor más alto de el coeficiente de Seebeck para el GaSe, ya que el valor máximo del coeficiente de Seebeck a 300 K para la región tipo$-p$ fue 1388 μV/K mientras que el valor obtenido para

la región tipo n es de 1294 μV/K. Estos valores son menores en el InSe e $InGaSe_2$.

- En el caso de una tetracapa, de todos los materiales estudiados $InGaSe_2$ exhibe los valores más altos del coeficiente Seebeck, dado que el valor máximo para la región tipo$-n$ en $InGaSe_2$ es de 3067.4082 μV/K, mientras para la región tipo$-p$ es de 3069.1 μV/K, valores menores que los del GaSe e InSe. En comparación con los casos del sistema en volumen, hubo una gran mejora en los valores del coeficiente de Seebeck para el caso de la tetracapa en todos los materiales estudiados. El aumento del coeficiente de Seebeck para el caso tetracapa podría atribuirse al fuerte efecto de confinamiento cuántico o el aumento local de la densidad total de estados a través de una estrecha gama de energía alrededor del nivel de Fermi en el caso de una tetracapa.

- En el marco de la teoría del transporte de Boltzmann (BT), suele adoptarse la aproximación del tiempo de relajación de dispersión constante (τ). En consecuencia, la conductividad eléctrica (σ) se expresa en mediante la relación (σ/τ). Con base en la estructura electrónica, la conductividad eléctrica se calculó en relación con el tiempo de relajación en función del potencial químico a temperatura ambiente para los tres materiales estudiados. Cuando el nivel de Fermi estaba en el centro de la banda prohibida, la conductividad eléctrica era cero. Pero cuando el nivel de Fermi comienza a moverse hacia arriba o hacia abajo en relación con el centro de la banda prohibida, la conductividad eléctrica comienza a aumentar a medida que aumenta el número de portadores de carga.

  - En el caso de la sistema en volumen σ/τ es alto en la región altamente dopada para ambas regiones, tipo$-p$ y tipo$-n$. Mientras que en GaSe e $InGaSe_2$ el valor máximo de σ/τ se ha obtenido en la región de tipo$-n$, se ha encontrado lo contrario en el caso del InSe. Dado que el valor máximo de σ/τ está en la región tipo$-p$.

Por tanto, el comportamiento general de σ/τ fue similar en todos los materiales estudiados en ambas regiones de tipo$-p$ y tipo$-n$.

  - En el caso de una tetracapa el intervalo en el que σ/τ es igual a cero ha aumentado en comparación con sus casos relativos en volumen. También el comportamiento de σ/τ en función del potencial químico en las regiones de tipo$-p$ y tipo$-n$ es diferente en cada material. Los valores de σ/τ son mayores en el sistema en volumen. Esto podría atribuirse a lo que se ha encontrado antes, que el valor de la densidad total de estados para el caso de volumen es mayor que la densidad total de estados para el caso tetracapa.

- Utilizando la información existente sobre el coeficiente de Seebeck (S) y la conductividad eléctrica relativa al tiempo de relajación (σ/τ), se puede obtener el factor de potencia relativo al tiempo de relajación ($PF/\tau = S^2\sigma/\tau$) en función del potencial quimico. Está claro que el factor de potencia es directamente proporcional al coeficiente de Seebeck y la conductividad eléctrica. Cerca del nivel de Fermi, el factor de potencia presenta los valores mínimos. Esto se atribuye a que σ/τ muestra los valores mínimos en la vecindad del nivel de Fermi.

  - En el caso de la sistema en volumen, de los tres casos investigados, el valor más alto de PF/τ se ha alcanzado en el $InGaSe_2$ de tipo$-p$.
  - En los casos de monocapa en todos los compuestos A pesar de que hay un gran aumento en los valores obtenidos para PF/τ en comparación con los casos en volumen, el intervalo donde PF/τ es igual a cero también se ha ampliado.

- La conductividad térmica total (κ) es la suma de la conductividad térmica electrónica (κ_e) y la conductividad térmica de los fonones (κ_l) i.e. $\kappa = \kappa_e + \kappa_l$. El codigo de BoltztraP calcula sólo la parte electrónica. Cuando el valor del potencial químico es cero, la conductividad térmica muestra su valor mínimo, que es casi cero y aumenta a medida que aumenta

el potencial. En el caso de las tetracapas todos los materiales exhiben valores inferiores de (κ/τ) en comparación con el caso en volumen.

Capítulo 6. Los coeficientes de transporte a alta presión

En este Capítulo se ha estudiado el efecto de la presión hidrostática sobre los coeficientes de transporte termoeléctrico del sistema en volumen de politipo $\varepsilon-$GaSe, InSe e $InGaSe_2$. En primer lugar, la estructura electrónica de los tres compuestos ha sido calculada mediante el código WIEN2k a tres presiones diferentes, 0, 10 y 20 GPa. Luego la información obtenida se ha insertado en el programa BoltzTraP para calcular los coeficientes de transporte en cada caso.

Resultados y discusión

- El efecto de la presión sobre el coeficiente de Seebeck de los materiales estudiados es diferente. Para el InSe a medida que la presión aumenta, los valores del coeficiente de Seebeck aumentan y también hay un aumento en el rango del potencial químico donde el coeficiente de Seebeck presenta un buen valor. Los mejores valores se han obtenido a 20 GPa, seguido por los valores a 10 GPa, mientras que los más bajos se han encontrado en 0 GPa. Esto significa que el coeficiente de Seebeck de InSe se puede mejorar aumentando la presión. El comportamiento fue diferente en GaSe y $InGaSe_2$, para ambos los mejores valores se encontraron a 10 GPa. Pero cuando la presión aumenta a 20 GPa, los valores del coeficiente de Seebeck empiezan a disminuir de nuevo. A pesar de que los valores para el $InGaSe_2$ la región n del GaSe son aún mejores que los calculados a 0 GPa, en la región p del GaSe, estos valores eran inferiores a los obtenido en 0 GPa.

- Se puede observar que el efecto de la presión sobre los valores de σ/τ es directo ya que en todos los casos estudiados los valores aumentan a medida que aumenta la presión. Por lo tanto, a partir de los resultados obtenidos del coeficiente de Seebeck y de la conductividad eléctrica, podemos decir que las propiedades termoeléctricas de los materiales estudiados podrían mejorarse aplicando presión sobre ellos.

- El aspecto general del efecto de la presión en todos los casos estudiados fue el aumento de los valores del factor de potencia para pequeños valores del potencial químico. A bajo dopaje, la mejora de los valores de PF/τ a menor potencial químico fue más pronunciada en la región de tipo n que en la región de tipo p.

  Para todos los materiales estudiados, cerca al nivel de Fermi los valores máximos de PF/τ fueron los calculados a 20 GPa mientras que en toda la gama estudiada del potencial químico, la presión a la cual se produce el máximo de PF/τ para cada material era diferente.

- El efecto de la presión en la conductividad térmica electrónica fue positivo es decir que los valores de la conductividad térmica para todos los materiales estudiados aumentan a medida que aumenta la presión. Por lo tanto, los valores más bajos de la conductividad térmica son los obtenidos a 0 GPa. Entonces aunque se produjo un aumento en los otros coeficientes de transporte con la presión, lo cual indicaría en principio que las propiedades termoeléctricas mejorarían con la presión, es el aumento de la conductividad térmica lo que hace que realmente tengamos un valor inferior de la figura de mérito.

References

[1] D. L. C. Chávez R. D. Chavez N. Scarlat J. Mahlknecht J. F. Dallemand G. S. A. Nava V. H. C. Flores and R. Parra. "Renewable energy research progress in Mexico: A review". In: *Renewable and Sustainable Energy Reviews* 32 (2014), pp. 140 –153.

[2] L. K. Samanta. "On some properties of I_2-IV-VI_3 compounds". In: *Phys. Status Solidi A* 100 (1987), K93 – K97.

[3] J. H. Yang H. J. Xiang X. G. Gong A. Walsh J. Kang Y. T. Zhai S. Chen and S.H. Wei. "Structural diversity and electronic properties of Cu_2SnX_3 (X=S, Se): A first-principles investigation". In: *Phys. Rev. B: Condens. Matter Mater. Phys.* 84 (2011), p. 075213.

[4] R. P. Rao G. H. Chandra O. L. Kumar and S. Uthanna. "Influence of substrate and selenization temperatures on the growth of Cu_2SnSe_3 films". In: *J. Mater. Sci.* 46 (2011), pp. 6952–6959.

[5] L. M. De Chalbaud D. B. Bracho G. Marcano C. Rincon and " G. Sanchez Perez. "Crystal growth and structure, electrical, and optical characterization of the semiconductor Cu_2SnSe_3". In: *J. Appl. Phys.* 90 (2001), 1847–1853.

[6] G. Jeffrey Snyder and E. S. Toberer. "Complex thermoelectric materials". In: *Nature Materials* 7 (2008), pp. 105–114.

[7] F. J. DiSalvo. "Thermoelectric Cooling and Power Generation". In: *Science* 285 (1999), pp. 703–706.

[8] T. Colpitts B.ÓQuinn R. Venkatasubramanian E. Siivola. In: *Nature* 413 (2001), pp. 597–602.

[9] T. M. Tritt. "Thermoelectric Phenomena, Materials, and Applications". In: *Annu. Rev. Mater. Res.* 41 (2011), p. 433.

[10] L. E. Bell. “Cooling, Heating, Generating Power, and Recovering Waste Heat with Thermoelectric Systems”. In: *Sci. Mag.* 321 (2008), pp. 1457–1461.

[11] D. Rowe. *handbook of thermoelectrics*. 1st edition. Boca Raton, FL: CRC Press, 1995.

[12] H. Alam and S. Ramakrishna. “A review on the enhancement of figure of merit from bulk to nano-thermoelectric materials”. In: *Nano Energy* 2 (2013), p. 190.

[13] H. Lee. “The Thomson effect and the ideal equation on thermoelectric coolers”. In: *Energy* 56 (2013), pp. 61–69.

[14] J. R. Szczech and S. Jin J. M. Higginsa. “Enhancement of the Thermoelectric Properties in Nanoscale and Nanostructured Materials”. In: *J. Mater. Chem.* 21 (2011), 4037–4055.

[15] G. Zhu B. Yu A. Minnich Y. Lan X. Wang M. Dresselhaus Z. Ren M. Zebarjadi G. Joshi and G. Chen. “Power Factor Enhancement by Modulation Doping in Bulk Nanocomposites.” In: *Nano Lett.* 11 (2011), 2225–2230.

[16] K. Esfarjani M. Dresselhaus M. Zebarjadi B. Liao and G. Chen. “Enhancing the Thermoelectric Power Factor by Using Invisible Dopants.” In: *Adv. Mater.* 25 (2013), 1577–1582.

[17] N. Mingo. “Thermoelectric Figure of Merit and Maximum Power Factor in $III^{\smile}V$ Semiconductor Nanowires.” In: *Appl. Phys. Lett.* 84 (2004), 2652–2654.

[18] S. Lee Z. Tian and G. Chen. “Heat Transfer in Thermoelectric Materials and Devices.” In: *J. Heat Transf.* 135 (2013), 061605–061605.

[19] D. M. Rowe. *Thermoelectrics Handbook: Macro to Nano*. CRC Press INC, 2006.

[20] B.-P. Zhang H.-L. Zhang W.-S. Liu L.-D. Zhao and J.-F. Li. “Enhanced thermoelectric property originating from additional carrier pocket in skutterudite compounds”. In: *Appl. Phys. Lett.* 93 (2008), p. 042109.

[21] Z. F. Ren A. J. Minnich M. S. Dresselhaus and G. Chen. "Bulk Nanostructured Thermoelectric Materials: Current Research and Future Prospects." In: *Energy Environ. Sci.* 2 (2009), p. 466.

[22] C. M. Bhandari and D. M. Rowe. "The Effect of Phonon-Grain Boundary Scattering, Doping and Alloying on the Lattice Thermal Conductivity of Lead Telluride." In: *Energy Environ. Sci.* 16 (1983), pp. L75–L77.

[23] I. D. Blum C.-I Wu-T. P. Hogan D. N. Seidman V. P. Dravid K. Biswas J. He and M. G. Kanatzidis. "High-Performance Bulk Thermoelectrics with All-Scale Hierarchical Architectures". In: *Nature* 489 (2012), 414–418.

[24] G. D. Mahan and J. O. Sofo. "The best thermoelectric". In: *Proc. Natl. Acad. Sci. USA* 93 (1996), pp. 7436–7439.

[25] J. O. Sofo and G. D. Mahan. "Optimum Band Gap of a Thermoelectric Material." In: *Phys. Rev. B* 49 (1994), 4565–4570.

[26] W. Hui-Qiong F. Zheyong and Z. Jin-Cheng. "Searching for the Best thermoelectrics through the Optimization of Transport Distribution Function." In: *J. Appl. Phys.* 109 (2011), p. 073713.

[27] A. LaLonde H. Wang-L. Chen-G. J. Snyder Y. Pei X. Shi. "Convergence of Electronic Bands for High Performance Bulk thermoelectrics." In: *Nature* 473 (2011), 66–69.

[28] M. Y. Tang-R. G. Yang H. Lee D. Z. Wang Z. F. Ren J. P. Fleurial M. S. Dresselhaus G. Chen and P. Gogna. "New Directions for Low-Dimensional Thermoelectric Materials." In: *Adv. Mater.* 19 (2007), 1043–1053.

[29] Y. Mune T. Mizoguchi-K. Nomura S. Ohta T. Nomura Y. Nakanishi Y. Ikuhara M. Hirano H. Hosono H. Ohta S. Kim and K. Koumoto. "Giant Thermoelectric Seebeck Coefficient of a Two-Dimensional Electron Gas in $SrTiO_3$". In: *Nat. Mater.* 6 (2007), 129–134.

[30] O. C. Calero M. M. González and P. D. Chao. "Nanoengineering thermoelectrics for 21st century: Energy harvesting and other trends in the field". In: *Renew. Sustain. Energy Rev.* 24 (2013), p. 288.

[31] E. S. Toberer-A. Saramat K. Kurosaki A. Charoenphakdee S. Yamanaka J. P. Heremans V. Jovovic1 and G. J. Snyder. "Enhancement of Thermoelectric Efficiency in PbTe by Distortion of the Electronic Density of States". In: *Science* 321.5888 (2008), pp. 554–557.

[32] Y. Lan K. Lukas-W. Liu K. Esfarjani C. Opeil D. Broido G. Chen Q. Zhang B. Liao and Z. Ren. "High thermoelectric performance by resonant dopant indium in nanostructured SnTe". In: *Proceedings of the National Academy of Sciences* 110.33 (2013), pp. 13261–13266.

[33] K. Yin H. Liu-X. Tang J. Shi Q. Zhang W. Liu X. Tan and C. Uher. "Convergence of Conduction Bands as a Means of Enhancing Thermoelectric Performance of n-Type $\mathrm{Mg_2Si_{1-x}Sn_x}$ Solid Solutions". In: *Phys. Rev. Lett.* 108 (2012), p. 166601.

[34] V. S. Shukla D. M. Rowe and N. Savvides. "Phonon scattering at grain boundaries in heavily doped fine-grained silicon–germanium alloys". In: *Nature* 290 (1981), pp. 765 –766.

[35] L. D. Hicks and M. S. Dresselhaus. "Effect of quantum-well structures on the thermoelectric figure of merit". In: *Phys. Rev. B* 47 (1993), pp. 12727–12731.

[36] T. Harman L. Hicks and M. Dresselhaus. In: *Appl. Phys. Lett.* 63 (1993), p. 3230.

[37] S. D. Guo and H. Ch. Li. "Monolayer enhanced thermoelectric properties compared with bulk for BiTeBr". In: *Computational Materials Science* 139 (2017), pp. 361–367.

[38] J. Tahir-Kheli J.-K. Yu W.A. Goddard III A.I. Boukai Y. Bunimovich and J.R. Heath. "Silicon nanowires as efficient thermoelectric materials." In: *Nature.* 451 (2008), pp. 168–171.

[39] E.V. Shevchenko-C.R. Kagan J.J. Urban D.V. Talapin and C.B. Murray. "Synergism in binary nanocrystal superlattices leads to enhanced p-type conductivity in self-assembled PbTe/Ag2 Te thin films." In: *Nat Mater.* 6 (2007), pp. 115–121.

[40] P. Hohenberg and W. Kohn. “Inhomogeneous Electron Gas”. In: *Phys. Rev.* 136 (1964), B864–B871.

[41] W. Kohn and L. J. Sham. “Self-Consistent Equations Including Exchange and Correlation Effects”. In: *Phys. Rev.* 140 (1965), A1133–A1138.

[42] M. Born and J.R. Oppenheimer. “On the Quantum Theory of Molecules”. In: *Ann. Phys.* 84 (1927), p. 457.

[43] G. Madsen-D. Kvasnicka P. Blaha K. Schwarz and J. Luitz. Wien2k: An augmented plane wave plus local orbitals program for calculating crystal properties users guide, 2014.

[44] B. R. Nag. *Electron Transport in Compound Semiconductors*. Springer Verlag, Berlin: John Wiley & Sons, Hoboken, 1980.

[45] P. B. Allen. *Boltzmann Theory and Resistivity of Metals, in Quantum Theory of Real Materials, edited by J. R. Chelikowsky and S. G. Louie*. Kluwer, Boston, 1996, pp. 219–250.

[46] J.M. Ziman. Oxford Classics Series. Oxford: Clarendon Press, 2001.

[47] C.M. Hurd. *The Hall Effect in Metals and Alloys*. New York-London: Plenum Press, 1972.

[48] Georg K.H. Madsen and David J. Singh. “BoltzTraP. A code for calculating band-structure dependent quantities”. In: *Computer Physics Communications* 175 (2006), pp. 67 –71.

[49] A.Brukl and G. Ortner. In: *Naturwiss.* 18 (1930), p. 393.

[50] W.C. Johnson and B. Warren. In: *Naturwiss.* 18 (1930), p. 666.

[51] W.Klemm and H. U. v. Vogel. In: *Z. Anorg. Allg. Chem.* 219 (1934), p. 45.

[52] H. Hahn. In: *Angew. Chem.* 65 (1953), p. 538.

[53] K.Schubert and E. Dörre. In: *Naturwiss.* 40 (1953), p. 604.

[54] K.Schubert and E. Dörre. In: *Naturwiss.* 41 (1954), p. 448.

[55] E. Dörre K.Schubert and M. Kluge. In: *Z. Metallkunde* 46 (1955), p. 216.

[56] S. A. Semiletov. In: *Sov. Phys. Cryst.* 3 (1958), p. 288.

[57] V.M. Salmanov Y. P. Sharonov G.A.Akhundov A. A. Agaeva and I. D. Yaroshetskii. In: *Sov. Phys. Semicond.* 7 (1973), p. 826.

[58] Y. F. Solomonov V. I. Sokolov and V. K. Sobashiev. In: *Sov. Phys.Solid State* 17 (1976), p. 1256.

[59] A. Minafra I. M. Catalano A. Cingolani and C. Paorici. "Second harmonic generation in layered compounds". In: *Opt. Commun.* 24 (1978), p. 105.

[60] Y. F. Solomonov and V. K. Sobashiev. "The Study of the Third Order Nonlinear Susceptibility in GaSe". In: *Phys. Status Solidi A* 74 (1982), pp. 75–78.

[61] M. E. Karaseev V. I.Konov L. A. Kulewskii N. B. Mustafaev P. P. Pashinin A. M. Prokhorov Y. M. Starodunov G. B. Abdullaev K. R. Allakverdiev and N. I. Chapliev. "Efficient generation of the second harmonic of CO_2 laser radiation in a GaSe crystal". In: *Sov. J. Quantum Electron.* 19 (1989), p. 494.

[62] A. Chevy A. Segura J.N. Besson and M.S. Martin. "Photovoltaic properties of GaSe and InSe junctions". In: *Nuovo Cimento Soc. Ital. Fis. B* 38 (1977), p. 345.

[63] A.R. Goñi A. Cantarero U.Schwarz V.Muñoz C. Ulrich M.A. Mroginski and K. Syassen. "Vibrational Properties of InSe under Pressure: Experiment and Theory". In: *Phys. Status Solidi B* 198 (1996), p. 121.

[64] A. Cantarero M. Hanfland U. Schwarz D. Olguín and K.Syassen. "Effect of pressure on the structural properties and electronic band structure of GaSe". In: *Phys. Status Solidi B* 244 (2007), pp. 244–255.

[65] H. L. Zhuang and R. G. Hennig. "Single-Layer Group-III Monochalcogenide Photocatalysts for Water Splitting". In: *Chem. Mater.* 25 (2013), pp. 3232–3238.

[66] N. D. Drummond V. Zólyomi and V. I. Falko. "Band structure and optical transitions in atomic layers of hexagonal gallium chalcogenides". In: *Phys. Rev.B* 87 (2013), p. 195403.

[67] M. Yoon X.-F. Qiao X. Zhang W. Feng P. Tan W. Zheng J. Liu X. Wang J. C. Idrobo D. B. Geohegan P. Hu J. Zhang and K. Xiao. "Highly sensitive phototransistors based on two- dimensional GaTe nanosheets with direct bandgap". In: *Nano Res.* 7 (2014), pp. 694–703.

[68] A. A. Puretzky J. C. Idrobo C. Ma M. Chi M. Yoon C. M. Rouleau I. I. Kravchenko D. B. Geohegan X. Li M.-W. Lin and K. Xiao. "Controlled Vapor Phase Growth of Single Crystalline, Two-Dimensional GaSe Crystals with High Photoresponse". In: *Sci. Rep.* 4 (2014), p. 5497.

[69] Y. Liu K. Yan J. Hong C. Jin Y. Zhou J.Yin Z. Liu Y. Zhou Y. Nie and H. Peng. "Epitaxy and Photoresponse of Two-Dimensional GaSe Crystals on Flexible Transparent Mica Sheets". In: *ACS Nano* 8 (2014), pp. 1485–1490.

[70] J. Hone J. Shan K. F. Mak Ch. Lee and T. F. Heinz. "Atomically Thin MoS_2: A New Direct-Gap Semiconductor". In: *Phys. Rev. Lett.* 105 (2010), p. 136805.

[71] A. Chevy A. Khun and R. Chevalier. "Crystal structure and interatomic distances in GaSe". In: *Phys. Status Solidi A* 31 (1975), p. 469.

[72] J. Etienne A. Likforman D. Carre and B. Bachet. In: *Acta Crystallogr., Sect. B: Struct. Crystallogr. Cryst. Chem.B* 31 (1975), p. 1252.

[73] K. Burke J. P. Perdew and M. Ernzerhof. "Generalized Gradient Approximation Made Simple". In: *Phys. Rev. Lett.* 77 (1996), pp. 3865–3868.

[74] K H Hellwege; O Madelung; M Schulz; H Weiss; W Freyland. *Crystal and solid state physics. Semiconductors. Physics of non-tetrahedrally bonded binary compounds*. Volume 17,Subvolume F Semiconductors : Physics of Non-Tetrahedrally Bonded Binary Compounds II. Springer Verlag, 1983.

[75] F. D. Murnaghan. "The Compressibility of Media under Extreme Pressures". In: *Proc. Natl. Acad. Sci. USA* 30 (1944), pp. 244–247.

[76] A. D. Becke and E. R. Johnson. "A simple effective potential for exchange". In: *J. Chem. Phys* 124 (2013), p. 221101.

[77] L. Hedin. "New Method for Calculating the One-Particle Green's Function with Application to the Electron-Gas Problem". In: *Phys. Rev.* 139 (1965), A796–A823.

[78] M. S. Hybertsen and S. G. Louie. "First-Principles Theory of Quasiparticles: Calculation of Band Gaps in Semiconductors and Insulators". In: *Phys. Rev. Lett.* 55 (1985), pp. 1418–1421.

[79] S. Hiadsi B. Abidri G. Vergoten L. Ghalouci B. Benbahi and F. Ghalouci. "First principle investigation into hexagonal and cubic structures of Gallium Selenide". In: *Computational Materials Science* 67 (2013), pp. 73–82.

[80] B. J. Zhao L. H. Xie S. R. Zhang S. F. Zhu and K. H. Song. "First-principles study of the elastic, electronic and optical properties of $\varepsilon-$GaSe layered semiconductor". In: *Physica B: Condensed Matter* 436 (2014), pp. 188 –192.

[81] M. Penzo K. Cenzual L.M. Gelato and E. Parthe. "Inorganic structure types with revised space groups. I". In: *Acta Cryst. B* 47 (1991), 433–439.

[82] M.N. Pyrlya S.V. Gavrilyuk M. Kaminskii Z.D. Kovalyuk and V.V. Netyaga. "Properties of Hydrogenated GaSe Crystals". In: *Inorg. Mater.* 41 (2005), 793–795.

[83] P. Perdew and Y. Wang. "Accurate and simple analytic representation of the electron-gas correlation energy". In: *Phys. Rev. B* 45 (1992), pp. 13244–13249.

[84] R. P. Alberto O. Daniel and C. Andrés. "Ab initio electronic band structure study of III-VI layered semiconductors". In: *The European Physical Journal B* 86.8 (2013), p. 350.

[85] O. Gunnarsson and K. Schönhammer. "Density-Functional Treatment of an Exactly Solvable Semiconductor Model". In: *Phys. Rev. Lett.* 56 (1986), p. 1968.

[86] M. S. Hybertsen and S. G. Louie. "Electron correlation in semiconductors and insulators: Band gaps and quasiparticle energies". In: *Phys. Rev. B* 34 (1986), p. 5390.

[87] M. Schlüter R. W. Godby and L. J. Sham. "Accurate Exchange-Correlation Potential for Silicon and Its Discontinuity on Addition of an Electron". In: *Phys. Rev. Lett.* 56 (1986), p. 2415.

[88] F. J. Manjón A. Chevy E. Machado G. Tobias P. Ordejón D. Errandonea A. Segura and E. Canadell. "Crystal symmetry and pressure effects on the valence band structure of $\gamma-$InSe and $\varepsilon-$GaSe: Transport measurements and electronic structure calculations". In: *Phys. Rev. B* 71 (2005), p. 125206.

[89] G. Meng Y. Lin M. Yandong D. Ying and H. Baibiao. "Tunable electronic and dielectric behavior of GaS and GaSe monolayers". In: *Phys. Chem. Chem. Phys.* 15 (2013), pp. 7098–7105.

[90] F. M. Gashimzade and N. B. Mustafaev. "Energy spectrum and effective mass of carriers in the InSe/GaSe superlattice". In: *Zeitschrift für Physik B Condensed Matter* 99 (1995), 219–222.

[91] H.Q. Wang Z.Y. Fan and J.C. Zheng. "Searching for the best thermoelectrics through the optimization of transport distribution function". In: *J. Appl. Phys.* 109 (2011), p. 073713.

[92] L. Reining G. Onida and A. Rubio. "Electronic excitations: density-functional versus many-body Green's-function approaches". In: *Rev. Mod. Phys.* 74 (2002), pp. 601–659.

[93] S. N. Rashkeev and W. R. L. Lambrecht. "Second-harmonic generation of I-III-VI_2 chalcopyrite semiconductors: Effects of chemical substitutions". In: *Phys. Rev. B* 63 (2001), p. 165212.

[94] M. S. Lee and S. D. Mahanti. "Validity of the rigid band approximation in the study of the thermopower of narrow band gap semiconductors". In: *Phys. Rev. B* 85 (2012), p. 165149.

[95] G. Pomrehn Y. Takagiwa Y. Pei and G. J. Snyder. "Validity of rigid band approximation of PbTe thermoelectric materials". In: *APL Mater.* 1 (2013), p. 011101.

[96] P. Pecheur H. Scherrer L. Jodin J. Tobola and S. Kaprzyk. "Effect of substitutions and defects in half-Heusler FeVSb studied by electron transport measurements and KKR-CPA electronic structure calculations". In: *Phys. Rev. B* 70 (2004), p. 184207.

[97] D. J. Singh and I. I. Mazin. "Calculated thermoelectric properties of La-filled skutterudites". In: *Phys. Rev. B* 56 (1997), R1650–R1653.

[98] D. F. Shao H. Y. Lu H. Y. Lv W. J. Lu and Y. P. Sun. "Strain-induced enhancement in the thermoelectric performance of a ZrS_2 monolayer". In: *J. Mater. Chem. C* 4 (2016), pp. 4538–4545.

[99] J. Sun and D. J. Singh. "Thermoelectric Properties of Mg_2(Ge,Sn): Model and Optimization of ZT". In: *Phys. Rev. Applied* 5 (2016), p. 024006.

[100] N. V. Chandra Shekar J. Sharp D. A. Polvani J. F. Meng and J. V. Badding. "Large Improvement in Thermoelectric Properties in Pressure-Tuned p-Type $Sb_{1.5}Bi_{0.5}Te_3$". In: *Chem. Mater.* 13 (2001), 2068–2071.

[101] W. Wlodarski S. Bhargava D. Akolekar A. Holland J. Tan K. Kalantar-zadeh and G. Rosengarten. "Thermoelectric properties of bismuth telluride thin films deposited by radio frequency magnetron sputtering". In: *Smart Sensors, Actuators, and MEMS II Carles Cane; Jung-Chih Chiao; Fernando Vidal Verdu, proceeding of SPIE* 5836 (2005).

[102] M. B. Sullivan X. Luo and S. Ying Quek. "First-principles investigations of the atomic, electronic, and thermoelectric properties of equilibrium and strained Bi_2Se_3 and Bi_2Te_3 including van der Waals interactions". In: *Phys. Rev. B* 86 (2012), p. 184111.

[103] A. H. Reshak. "Thermoelectric properties of fully hydrogenated graphene: Semi-classical Boltzmann theory". In: *Journal of Applied Physics* 117 (2015), p. 225104.

[104] L. D. Hicks and M. S. Dresselhaus. "Thermoelectric figure of merit of a one-dimensional conductor". In: *Phys. Rev. B* 47 (1993), pp. 16631–16634.

[105] D. T. Morelli J. P. Heremans C. M. Thrush and M.-Ch. Wu. "Thermoelectric Power of Bismuth Nanocomposites". In: *Phys. Rev. Lett.* 88 (2002), p. 216801.

[106] D. Guo and C. Hu. "Ultrahigh thermoelectricity of atomically thick Bi2Se3 single layers: A computational study". In: *Applied Surface Science* 321 (2014), pp. 525 –530.

[107] T. Thonhauser J. V. Badding T. J. Scheidemantel C. Ambrosch-Draxl and J. O. Sofo. "Transport coefficients from first-principles calculations". In: *Phys. Rev. B* 68 (2003), p. 125210.

[108] T.J. Scheidemantel T. Thonhauser and J.O. Sof. "Improved thermoelectric devices using bismuth alloys". In: *Appl. Phys. Lett.* 85 (2004), pp. 588–590.

[109] L. Bertini and C. Gatti. "The impact of the actual geometrical structure of a thermoelectric material on its electronic transport properties: the case of doped skutterudite systems." In: *J. Chem. Phys.* 121 (2004), pp. 8983–8989.

[110] W. E. Pickett P. B. Allen and H. Krakauer. "Anisotropic normal-state transport properties predicted and analyzed for high-T_c oxide superconductors". In: *Phys. Rev. B* 37 (1988), pp. 7482–7490.

[111] Q. Zhang W. Liu B. Yu H. Wang D. Wang G. Ni G. Chen Q. Zhang H. Wang and Z. Ren. "Effect of Silicon and Sodium on Thermoelectric Properties of Thallium-Doped Lead Telluride-Based Materials". In: *Nano Lett.* 12 (2012), 2324–2330.

[112] F. Dang T. Itoh Y. Wang H. Sasaki M. Kondo K. Koga K. Yabuki G. Snyder R. Yang C. Wang X. Gu and K. Koumoto. "Flexible n-type thermoelectric materials by organic intercalation of layered transition metal dichalcogenide TiS_2". In: *Nat Mater.* 14 (2015), 622–627.

[113] W. Liu1 et al. "Importance of high power factor in thermoelectric materials for power generation application: A perspective". In: *Scripta Mater* 111 (2016), 3–9.

[114] C. Kittel. *Introduction to Solid State Physics*. nifth. New York City: John Wiley & Sons, Hoboken, 2004.

[115] S.J. Asadabadi R. Ahmad M. Bilal I. Ahmad and M. Maqbool. "Thermoelectric properties of metallic antiperovskites AXD_3 (A=Ge, Sn, Pb, Al, Zn, Ga; X=N, C; D=Ca, Fe, Co)". In: *Electron. Mater. Lett.* 11 (2015), 466–480.